The Astrophysical Journal, 957:88 (23pp), 2023 November 10 https://doi.org/10.3847/1538-4357/acf863

Astrochemical Modeling of Propargyl Radical Chemistry in TMC-1

Alex N. Byrne[1], Ci Xue[1], Ilsa R. Cooke[2], Michael C. McCarthy[3], and Brett A. McGuire[1,4]
[1] Department of Chemistry, Massachusetts Institute of Technology, Cambridge, MA 02139, USA; lxbyrne@mit.edu
[2] Department of Chemistry, University of British Columbia, 2036 Main Mall, Vancouver, BC V6T 1Z1, Canada
[3] Center for Astrophysics | Harvard & Smithsonian, Cambridge, MA 02138, USA
[4] National Radio Astronomy Observatory, Charlottesville, VA 22903, USA

Received 2023 May 3; revised 2023 September 5; accepted 2023 September 7; published 2023 November 2

Abstract

Recent detections of aromatic species in dark molecular clouds suggest that formation pathways may be efficient at very low temperatures and pressures, yet current astrochemical models are unable to account for their derived abundances, which can often deviate from model predictions by several orders of magnitude. The propargyl radical, a highly abundant species in the dark molecular cloud TMC-1, is an important aromatic precursor in combustion flames and possibly interstellar environments. We performed astrochemical modeling of TMC-1 using the three-phase gas-grain code `NAUTILUS` and an updated chemical network, focused on refining the chemistry of the propargyl radical and related species. The abundance of the propargyl radical has been increased by half an order of magnitude compared to the previous GOTHAM network. This brings it closer in line with observations, but it remains underestimated by 2 orders of magnitude compared to its observed value. Predicted abundances for the chemically related C_4H_3N isomers within an order of magnitude of observed values corroborate the high efficiency of CN addition to closed-shell hydrocarbons under dark molecular cloud conditions. The results of our modeling provide insight into the chemical processes of the propargyl radical in dark molecular clouds and highlight the importance of resonance-stabilized radicals in polycyclic aromatic hydrocarbon formation.

Unified Astronomy Thesaurus concepts: Astrochemistry (75); Polycyclic aromatic hydrocarbons (1280); Radical-radical recombination (1071); Chemical kinetics (2233); Molecular clouds (1072)

1. Introduction

Polycyclic aromatic hydrocarbons (PAHs) are the probable carriers of the unidentified infrared emission bands pervasive in our and other galaxies (Tielens 2008), as well as potentially some of the diffuse interstellar bands that can be observed in the infrared, visible, and ultraviolet (UV) spectra of the interstellar medium (ISM; Duley 2006). Despite the ubiquity of these molecules in the ISM, their formation pathways remain ambiguous. One suggested formation route is through high-temperature growth processes in the circumstellar envelopes of evolved stars followed by injection into the ISM (Tielens 2008; Kaiser & Hansen 2021). However, in the diffuse ISM and photodissociation regions, carbonaceous material on dust grains and in the gas phase is exposed to UV photon irradiation and shocks (Berné et al. 2015). It is thought that small PAHs of less than 20–30 atoms often cannot internally redistribute energy from the absorption of UV photons in such regions or reradiate it back out before they are destroyed, resulting in short lifetimes (Chabot et al. 2019). Recent observations of the Taurus Molecular Cloud (TMC-1) reported the detection of benzonitrile (McGuire et al. 2018), the first six-membered aromatic ring detected via radio astronomy, followed by detection of the small PAHs 1- and 2-cyanonaphthalene, indene, and 2-cyanoindene (Burkhardt et al. 2021a; McGuire et al. 2021; Sita et al. 2022). While the discovery of aromatic molecules in dark molecular clouds appears to imply the existence of efficient low-temperature formation routes, current astrochemical models dramatically fail to reproduce their observed abundances. This gap in our understanding of aromatic chemistry highlights the need for further exploration of the formation and chemical evolution of these molecules.

Several theoretical and experimental studies have proposed gas-phase formation pathways to benzene (C_6H_6) from small hydrocarbons (Hébrard et al. 2006; Jones et al. 2011; Caster et al. 2019). In combustion flames, benzene and the phenyl radical are suggested to be efficiently formed from the recombination of two propargyl radicals (CH_2CCH; Miller & Melius 1992)

$$\begin{aligned} CH_2CCH + CH_2CCH &\rightarrow C_6H_6 \\ &\rightarrow C_6H_5 + H. \end{aligned} \tag{1}$$

CH_2CCH is a small, resonance-stabilized hydrocarbon radical (as shown in Figure 1) that can form in flames from the insertion of an electronically excited methylene radical ($^1CH_2$) into the C–H bond of C_2H_2(Miller & Melius 1992). Computational studies of the C_6H_6 potential energy surface have shown that two propargyl radicals can barrierlessly combine and undergo decomposition to form o-benzyne (c-C_6H_4) + H_2 or phenyl radical (C_6H_5) + H, with the latter pathway expected to be the dominant bimolecular pathway (Miller & Klippenstein 2003b). Experimental studies at high temperatures have revealed the formation of o-benzyne and the C_6H_6 isomers benzene, fulvene, 1,5-hexadiyne, and 2-ethynyl-1,3-butadiene (Zhao et al. 2021). The product branching ratios were found to heavily depend on temperature and pressure, providing critical information about formation of aromatic species in combustion flames and in dense environments such as Titan's atmosphere (Zhao et al. 2021). In contrast, the C_6H_5 + H channel is expected to prevail in cold and less dense

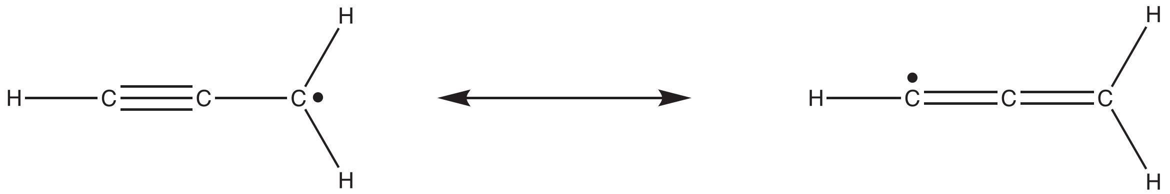

Figure 1. Resonance structures of CH_2CCH.

environments such as TMC-1, whereas the c-C_6H_4 channel is expected to be negligible. While previous astrochemical studies have placed an emphasis on benzene as the first aromatic ring formed en route to PAH formation (Jones et al. 2011; Caster et al. 2019), these studies of CH_2CCH recombination indicate that the phenyl radical may be equally important. In order to better model and understand aromatic chemistry of interstellar environments, a greater emphasis must be placed on alternative formation pathways involving C_6H_5, beginning with CH_2CCH recombination.

The detection of CH_2CCH in TMC-1 at millimeter wavelengths has further spurred astrochemical interest in the molecule (Agúndez et al. 2021, 2022). An observed abundance of 1.0×10^{-8} with respect to molecular hydrogen makes this one of the most abundant radicals detected in TMC-1, with a CH_3CCH/CH_2CCH ratio approximately equal to 1 (Agúndez et al. 2022). In addition to the detection of CH_2CCH, the authors performed an astrochemical modeling study of the radical and its closed-shell counterparts. They concluded that the major contributions to the production of CH_2CCH include the neutral–neutral reaction between ethylene (C_2H_4) and atomic carbon in the gas phase,

$$C_2H_4 + C \rightarrow CH_2CCH + H, \tag{2}$$

and the dissociative recombination (DR) reactions of 3-carbon cations,

$$C_3H_n^+ + e^- \rightarrow CH_2CCH + (n - 3)H, \tag{3}$$

where $n = 4$, 5, and 6. The major destruction pathways were found to be reactions with neutral atoms such as C, O, and N. While this model reproduced the observed abundance of the closed-shell species CH_3CCH well, the modeled propargyl abundance was underestimated by over 2 orders of magnitude. The presence of low-temperature kinetic measurements for a number of relevant neutral–neutral reactions is a significant benefit toward understanding the chemistry of this radical under molecular cloud conditions (Slagle et al. 1991; Canosa et al. 1997, 2007; Chastaing et al. 1999, 2000), but the sizable difference between observed and modeled abundances indicates that existing gas-phase reactions may need to be reevaluated. In particular, experimental studies of the reactions between CH_2CCH and neutral atoms at low temperatures are rare. Moreover, a main limitation of the astrochemical model presented in Agúndez et al. (2021) is the lack of consideration for grain chemistry. Hickson et al. (2016) revealed that surface hydrogenation of 3-carbon hydrocarbons on interstellar grains may be critical for the formation of CH_2CCH and its closed-shell counterparts.

The high abundance of CH_2CCH despite its open-shell nature and its close connection to aromatic species highlight it as an important species in the chemical evolution of molecular clouds, yet previous astrochemical knowledge on this species was incomplete. Detailed kinetic studies at low temperature provide the most relevant information for modeling the chemistry of dark molecular clouds and other interstellar regions (Hébrard et al. 2009), but the sheer number of possible reactions and the difficulty in replicating interstellar conditions make this a formidable problem. In order to investigate the chemical evolution of CH_2CCH in the ISM, we performed astrochemical modeling under dark cloud conditions with an updated and expanded chemical network. In Section 2, we describe the modeling code and physical conditions used, as well as the modifications made to the chemical network. The results of the modeling efforts toward CH_2CCH and related species are presented in Section 3. Finally, we discuss these results in Section 4, along with comparisons to previous works and future directions.

2. Methods

The astrochemical modeling code utilized is `NAUTILUS`, a three-phase gas-grain rate equation model (Ruaud et al. 2016). The gas phase, grain surface, and grain mantle are treated individually with their own parameters and chemical reactions. Additional physical processes of diffusion between grain surface and mantle, diffusion within grain surface and mantle, adsorption of gas-phase species onto the grain, and desorption of grain-surface species into the gas phase are considered. Additionally, the `NAUTILUS` model considers photodissociation and photodesorption by external UV photons and cosmic-ray-induced UV photons, thermal evaporation, evaporation via cosmic-ray stochastic heating, and chemical desorption. We used the default 1% efficiency for the chemical desorption mechanism and a peak grain temperature of 70 K for 1×10^{-5} yr for the cosmic-ray heating mechanism. More information on these mechanisms and their implementations can be found in the `NAUTILUS` documentation,[5] as well as Ruaud et al. (2016) and references therein.

The physical conditions chosen were those of a standard cold molecular cloud, namely a gas density of 2×10^4 cm^{-3} (Snell et al. 1982), a kinetic temperature of 10 K for both gas and dust (Pratap et al. 1997), a cosmic-ray ionization rate of 1.3×10^{-17} s^{-1} (Spitzer & Tomasko 1968), and a visual extinction of 10 mag (Rodríguez-Baras et al. 2021). The initial elemental abundances used, which are listed in Table 1 along with their references, were the low metal abundances of Graedel et al. (1982) with a few modifications. In particular, the ratio of initial carbon abundance to initial oxygen abundance (C/O ratio) has been found to have a noticeable effect on the modeled chemistry, with long carbon chains being the most affected (Hincelin et al. 2011). It has been found that a C/O ratio of 1.1 due to a lowered initial abundance of atomic

---

[5] https://forge.oasu.u-bordeaux.fr/LAB/astrochem-tools/pnautilus/-/blob/master/pnautilus_documentation.pdf

Table 1
Initial Atomic/Molecular Abundances with Reference to Atomic Hydrogen

Species	n/n_H	References	Species	n/n_H	References
H_2	0.499	Ruaud et al. (2016)	F	6.68×10^{-9}	Neufeld et al. (2005)
He	0.09	Wakelam & Herbst (2008)	Cl	1.00×10^{-9}	Graedel et al. (1982)
C	1.70×10^{-4}	Jenkins (2009)	Si	8.00×10^{-9}	Graedel et al. (1982)
N	6.20×10^{-5}	Jenkins (2009)	Na	2.00×10^{-9}	Graedel et al. (1982)
O	1.55×10^{-4}	Xue et al. (2020)	Mg	7.00×10^{-9}	Graedel et al. (1982)
S	7.50×10^{-7}	Fuente et al. (2023)	Fe	3.00×10^{-9}	Graedel et al. (1982)
P	2.00×10^{-10}	Graedel et al. (1982)	…	…	…

oxygen significantly improves the general agreement between modeled and observed abundances of carbon-chain molecules in TMC-1 (Xue et al. 2020; Loomis et al. 2021). Additionally, a depletion factor of 20 with respect to the solar abundance for sulfur has been used according to a recent study based on data from the GEMS survey (Fuente et al. 2023).

Based on kida.uva.2014 (Wakelam et al. 2015), the chemical network was extended to include aromatic and carbon-chain networks in the Green Bank Telescope Observations of TMC-1: Hunting for Aromatic Molecules (GOTHAM) project (McGuire et al. 2018, 2020, 2021; Xue et al. 2020; Loomis et al. 2021; McCarthy et al. 2021). To compare and contrast, we present the model results of CH_2CCH and its related species with both the default network used in previous GOTHAM analyses (without any of the changes new to this work, hereafter referred to as GOTHAM DR1) and a modified network, as detailed below.[6]

2.1. Formation Mechanisms of CH_2CCH

To better represent the chemical evolution of CH_2CCH and its closed-shell counterparts in cold molecular clouds, an extensive literature search and analysis were performed to identify new reactions and to examine existing reactions. In general, low-temperature and low-density laboratory kinetic studies provide the most accurate rate information for astrochemical models (Hébrard et al. 2009). In the absence of these, theoretical data and/or high-temperature experimental data are taken into account with caution when extrapolating high-temperature kinetic data to low temperatures such as 10 K. For example, rate constants estimated from high-temperature data could be inaccurate by multiple orders of magnitude if there is a U-shaped temperature dependence (Jiménez et al. 2016). Since previous astrochemical models underestimated the peak abundance of CH_2CCH, a special focus was placed on the production mechanisms of this species.

2.1.1. Dissociative Recombination

DR reactions of molecular cations with electrons are essential to interstellar chemistry owing to their high efficiency under low-temperature and low-density conditions (Geppert et al. 2004; Florescu-Mitchell & Mitchell 2006). In our current chemical model, we considered four different species that produce CH_2CCH via DR, namely the DR reactions of $C_3H_4^+$, $C_3H_5^+$, $C_5H_5^+$, and $C_4H_7^+$. The $C_3H_4^+$ DR reaction was investigated experimentally by Geppert et al. (2004), finding a large preference for the formation of CH_2CCH. The branching ratios determined from this experiment were adopted here, along with an overall rate constant from Florescu-Mitchell & Mitchell (2006). Angelova et al. (2004) studied the DR reaction of $C_3H_5^+$ and found that products containing C_3 species account for 86.7% of products, with C_2-containing products accounting for the remaining 13.3%. The individual branching ratios and overall rate constant were determined by Loison et al. (2017) using information from photodissociation studies of the neutral species. The last two species, $C_5H_5^+$ and $C_4H_7^+$, have not received experimental study and have been assumed to produce CH_2CCH with branching ratios of 50% and 65%, respectively, based on enthalpies of reaction. A full list of changes to DR reactions implemented in our updated model is shown in Table 4 in Appendix A.

2.1.2. Ion–Neutral Reactions

In addition to DR reactions, reactions between ions and neutral molecules account for a significant portion of interstellar chemistry owing to relatively large reaction rates, the frequent absence of activation energies, and a variety of abundant interstellar ions (Friedman 1968). Rate constants for ion–molecule reactions can be estimated according to capture theories such as Equations (4)–(6), the Su–Chesnavich formulae (Su & Chesnavich 1982; Woon & Herbst 2009),

$$x = \frac{\mu_D}{\sqrt{2\alpha k_B T}} \tag{4}$$

$$k_D = 2\pi e\sqrt{\frac{\alpha}{\mu}}(0.4767x + 0.6200) \tag{5}$$

$$k_D = 2\pi e\sqrt{\frac{\alpha}{\mu}}\left(\frac{(x + 0.5090)^2}{10.526} + 0.9754\right). \tag{6}$$

These expressions are an empirical fit to classical trajectory calculations, where k_D is the ion–neutral rate constant, μ_D is the dipole moment, α is the polarizability, k_B is the Boltzmann constant, e is the charge of an electron, and μ is the reduced mass. The parameter x is a unitless value that determines which expression is used for calculation of a rate coefficient. When $x \geqslant 2$, k_D increases linearly with x and Equation (5) is used. When $x < 2$, the relationship between k_D and x is quadratic and Equation (6) is used. If $x = 0$, the expression is reduced to the Langevin rate,

$$k_L = 2\pi e\sqrt{\frac{\alpha}{\mu}}, \tag{7}$$

the classical rate constant for the reaction between an ion and a nonpolar neutral molecule. For many polar molecules, this value is greater than 2 over the temperature range of interest (10–300 K). For CH_2CCH, however, $x < 2$ over this temperature range owing to its small dipole moment of 0.150 D (Küpper et al. 2002).

---

[6] A Zenodo repository containing the input files for our updated network can be found at doi:10.5281/zenodo.8320140.

Table 2
Polarizabilities and Dipole Moments for Updated Ion–Neutral Reactions

Molecule	Polarizability (Å)	Dipole Moment (D)	References[a]
CH_2CCH	5.556	0.150	Woon & Herbst (2009), Küpper et al. (2002)
$CNCH_2CCH$	7.175	3.61	Woon & Herbst (2009), McNaughton et al. (1988)
CH_2CCHCN	8.136	4.28	Woon & Herbst (2009), Bouchy et al. (1973)
CNCHCHCCH	…	5.00	Lee et al. (2021)
CNCHCCH	…	5.47	Cabezas et al. (2022)

Note.
[a] References for polarizability are listed first, followed by references for dipole moment, unless there is no polarizability value.

In our reaction network, three neutral species, namely $CNCH_2CCH$, CNCHCHCCH, and CNCHCCH, can generate CH_2CCH via reaction with abundant cations. For $CNCH_2CCH$ and CNCHCHCCH, it was assumed that reactions with H^+, H_3^+, He^+, C^+, HCO^+, and H_3O^+ all form CH_2CCH. For CNCHCCH, only reactions with H^+ and H_3^+ were considered to contribute to the formation of CH_2CCH, as He^+ and C^+ do not contain hydrogen and reactions with HCO^+ and H_3O^+ were assumed to produce l-C_3H_2 instead. Ion–neutral rate coefficients were reevaluated for each of these species using Equation (5) and the μ_D and α values in Table 2. For species without experimental or calculated polarizabilities, the rate constant was estimated by adding a negative temperature dependence to the polarizability-independent term. The results of these calculations are listed in Table 6 in Appendix B.

In our network, $CNCH_2CCH$ and CNCHCHCCH can be formed directly or indirectly from reactions involving CH_2CCH. In order to ensure that these ion–neutral reactions were not generating a loop of net-zero loss and arbitrarily inflating the abundance of CH_2CCH, we tested the effect of these reactions on modeled abundances by varying only the products. These alternate products were taken from Quan & Herbst (2007).

2.1.3. Neutral–Neutral Reactions

While collisions between two neutral molecules may not be as efficient at low temperatures owing to a lack of strong attractive forces and the possibility of energy barriers, it has been shown that some of these reactions play a crucial role in the chemistry of molecular clouds (Chastaing et al. 1999; Carty et al. 2001). The reaction

$$CH + C_2H_4 \rightarrow CH_3CCH + H \tag{8}$$

has been studied experimentally by Goulay et al. (2009) using time-resolved vacuum UV ionization mass spectrometry at room temperature, finding that 30% of the detected products were CH_3CCH. Kinetic studies of this reaction were performed by Canosa et al. (1997) between 23 and 298 K using the CRESU experimental setup. This technique, developed by Rowe et al. (1984), uses Laval nozzles to create a uniform flow of gas at temperatures as low as 10 K without precooling, making it ideal for studying the kinetics of astrochemical reactions (Cooke & Sims 2019; Hays et al. 2022). We therefore updated this reaction to reflect the experimental branching ratio and 23 K rate coefficient. Additionally, the radical–radical reaction

$$CCH + CH_3 \rightarrow CH_2CCH + H \tag{9}$$

was added to the network with a rate coefficient estimated by Loison et al. (2017). Finally, we have incorporated the rate coefficient for the reaction

$$C_2 + CH_4 \rightarrow CH_2CCH + H \tag{10}$$

as measured experimentally at 24 K by Canosa et al. (2007), again using the CRESU technique. The rate coefficients are listed in Table 7 in Appendix C.

2.2. Destruction Mechanisms of CH_2CCH

For a full chemical description of CH_2CCH and its counterparts, it is also necessary to investigate the relevant destruction mechanisms. As with the production mechanisms, an extensive literature search was performed with a priority toward low-temperature kinetic experiments.

2.2.1. Ion–Neutral Reactions

Analogous to many other polar neutral species discussed in Section 2.1.2, CH_2CCH is assumed to be destroyed mainly by reacting upon collision with cations in dense molecular clouds. The rate coefficients are well described by the Su–Chesnavich formalism. In addition to abundant cations such as H_3^+ and HCO^+, a range of complex hydrocarbon cations such as $C_2H_2^+$ and $C_3H_4^+$ were also considered. These rates have been recalculated as required using Equation (6) with the dipole and polarizability values from Table 2 and are summarized in Table 5 in Appendix B.

2.2.2. Neutral–Neutral Reactions

In addition to cations, CH_3CCH and CH_2CCH can be destroyed by reaction with atoms and small molecules at low temperatures. The reaction between CH_3CCH and C has been studied at room temperature by Loison & Bergeat (2004) with a fast-flow reactor and resonance fluorescence and down to 15 K by Chastaing et al. (1999) with the CRESU apparatus. Loison & Bergeat (2004) observed a hydrogen production ratio of 85% corresponding to the $H + C_4H_3$ product channel, with the remaining 15% most likely attributed to the $H_2 + C_4H_2$ channel. These branching ratios, along with the 15 K rate coefficient, were adopted into our chemical network.

For CH_2CCH, reactions with H, O, N, and OH are of interest. Theoretical studies of the C_3H_4 potential energy surface have shown the presence of activation barriers for the reactions

$$CH_2CCH + H \rightarrow c\text{-}C_3H_2 + H_2 \tag{11}$$

and

$$CH_2CCH + H \rightarrow l\text{-}C_3H_2 + H_2. \tag{12}$$

As such, they are unlikely to be viable mechanisms under cold dense cloud conditions (Miller & Klippenstein 2003a). The radiative association reaction

$$CH_2CCH + H \rightarrow CH_3CCH + h\nu, \tag{13}$$

however, is barrierless and feasible under interstellar conditions (Hébrard et al. 2013). As such, the rate coefficient and branching ratio for this reaction have been updated according to Loison et al. (2017). The $CH_2CCH + O$ reaction rate has been studied from 295 to 750 K using a heatable flow reactor and photoionization mass spectrometry but did not show any temperature dependence in this range (Slagle et al. 1991). The branching ratios for the products have been assigned based on theoretical studies (Loison et al. 2017). Due to a lack of experimental or theoretical data, the rate coefficient and branching ratios for the reaction of CH_2CCH with N have been estimated based on the $N + C_2H_3$ reaction (Loison et al. 2017). For the $CH_2CCH + OH$ reaction, we use a temperature-independent estimate from Hansen et al. (2009) for the overall rate coefficient, with assumed 50/50 branching ratios between the two product channels. These reactions have all been implemented in our updated chemical network and are listed with the rate coefficients in Table 7 in Appendix C.

The self-recombination between propargyl radicals, Reaction (1), has been the subject of multiple kinetic studies at room temperature and above. Atkinson & Hudgens (1999), Fahr & Nayak (2000), and DeSain & Taatjes (2003) have all measured the rate constant of this reaction at room temperature and for pressures of 2.25–100 torr, 50 torr, and 16 torr, respectively. The results of these three experiments agree well on a room-temperature rate constant of $\sim 4.0 \times 10^{-11}$ $cm^3 s^{-1}$ at the high-pressure limit. There has not yet been any experimental low-temperature study of the propargyl radical recombination; however, a theoretical study by Georgievskii et al. (2007) used variable reaction coordinate transition state theory (VRC-TST) to determine the temperature dependence of this reaction in the high-pressure limit. These calculations agree well with the aforementioned experiments and suggest a slight negative temperature dependence, leading to a rate constant that is only slightly larger ($\sim 6.0 \times 10^{-11}$ $cm^3 s^{-1}$) at 10 K. We adopt the experimental value of 4×10^{-11} $cm^3 s^{-1}$ into our network as an estimate. The branching ratios under conditions relevant to TMC-1 are not known either; however, Miller & Klippenstein (2003b) estimated that $C_6H_5 + H$ is the dominant bimolecular exit channel owing to a barrierless reverse association and low-energy transition state, contrary to the $c\text{-}C_6H_4 + H_2$ exit channel. In our network, we assumed that $C_6H_5 + H$ are the only products of this reaction, and thus we implement the reaction

$$CH_2CCH + CH_2CCH \rightarrow C_6H_5 + H. \tag{14}$$

2.3. Incorporation of CH_2CCH_2

Of the two linear closed-shell isomers of C_3H_4, CH_3CCH and CH_2CCH_2, only the former species was previously considered in the chemical network. As with CH_3CCH, CH_2CCH_2 is a closed-shell counterpart of CH_2CCH, and thus these species are likely linked chemically. Our model has been updated to produce CH_2CCH_2 through three reaction paths, including the DR reaction

$$C_3H_5^+ + e^- \rightarrow CH_2CCH_2 + H, \tag{15}$$

the radiative association reaction

$$H + CH_2CCH \rightarrow CH_2CCH_2 + h\nu, \tag{16}$$

and the neutral–neutral reaction

$$C_2H_4 + CH \rightarrow CH_2CCH_2 + H \tag{17}$$

(Canosa et al. 1997; Goulay et al. 2009; Loison et al. 2017). The last reaction also has a $CH_3CCH + H$ product channel that was already included in the network. For the radiative association of CH_2CCH with H, we assume 50/50 branching ratios for the C_3H_4 isomers owing to the lack of low-temperature information, in line with Loison et al. (2017).

Destruction pathways of CH_2CCH_2 include reaction with atomic carbon as measured down to 15 K by Chastaing et al. (1999), reaction with CCH as measured down to 63 K by Carty et al. (2001), and reaction with CH as measured down to 77 K by Daugey et al. (2005). Additional ion–neutral destruction pathways have also been included (Loison et al. 2017). Some interstellar species are capable of isomerization with assistance from collisions with H and H_2. However, the interconversion of the two C_3H_4 species has barriers in both directions of a few kcal mol^{-1}, enough to make them negligible under TMC-1 conditions (Narendrapurapu et al. 2011).

2.4. Reactions with CN Radicals

Laboratory studies at low temperature and density suggest that the formation of CN-substituted hydrocarbons via reaction with CN radicals is efficient under dark molecular cloud conditions (Carty et al. 2001; Cooke et al. 2020). There are three isomers of C_4H_3N: propargyl cyanide ($CNCH_2CCH$), cyanoallene (CH_2CCHCN), and methylcyanoacetylene (CH_3C_3N) as shown in Figure 2, all of which have been detected in TMC-1 (Broten et al. 1984; Lovas et al. 2006; McGuire et al. 2020). In particular, McGuire et al. (2020) assumed $CNCH_2CCH$ to be formed as the major product from the reaction between CN and CH_3CCH. However, Balucani et al. (2002) estimated a 50/50 branching ratio of CH_2CCHCN/CH_3C_3N based on crossed molecular beam experiments and electronic structure calculations. Additionally, Abeysekera et al. (2015) investigated this reaction via chirped-pulse/uniform flow microwave spectroscopy and observed that CH_3C_3N is the only C_4H_3N isomer formed, along with HC_3N and CH_2CCH,

$$\begin{aligned} CN + CH_3CCH &\rightarrow HC_3N + CH_3 && 66\% \\ &\rightarrow CH_3C_3N + H && 22\% \\ &\rightarrow HCN + CH_2CCH && 12\%. \end{aligned} \tag{18}$$

We therefore modified this reaction based on the branching ratios from Abeysekera et al. (2015) and the rate coefficient from Carty et al. (2001).

The reaction between CN and CH_2CCH_2 can also form C_4H_3N isomers. Using the same procedure as the $CN + CH_3CCH$ reaction, Balucani et al. (2002) suggested that CH_2CCHCN is the major product of this reaction, with $CNCH_2CCH$ being the minor product,

$$\begin{aligned} CN + CH_2CCH_2 &\rightarrow CH_2CCHCN + H, && 90\% \\ &\rightarrow CNCH_2CCH + H && 10\%. \end{aligned} \tag{19}$$

This reaction was introduced to our network with the above branching ratios from Balucani et al. (2002) and the rate coefficient from Carty et al. (2001). As CH_2CCHCN had previously not been included in our network, destruction pathways via reaction with abundant interstellar ions were included analogous to $CNCH_2CCH$. The rates for these

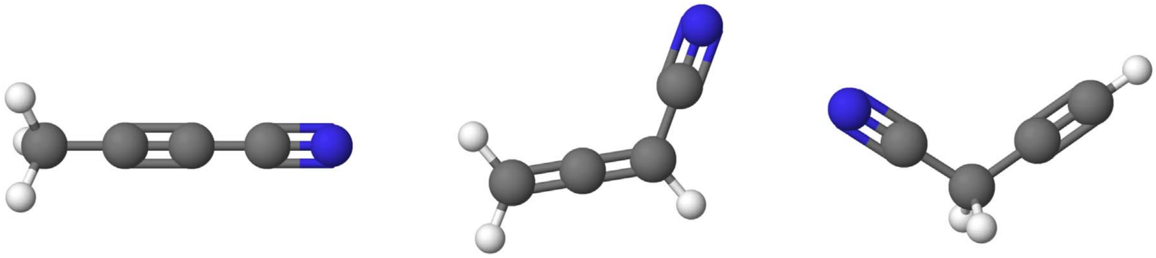

Figure 2. Chemical structures of the three isomers of C_4H_3N that have been detected in TMC-1: methylcyanoacetylene (left), cyanoallene (middle), and propargyl cyanide (right).

reactions were calculated using Equation (5) and the dipole and polarizability in Table 2. As with $CNCH_2CCH$, we tested alternate ion–neutral products from Quan & Herbst (2007) to avoid arbitrarily inflating the abundance of CH_2CCH and related species.

There is limited information on the reaction between CN and CH_2CCH. Although Cabezas et al. (2021) proposed 3-cyano propargyl radical (CH_2C_3N) as the main product, radical–radical reactions involving CN may not follow the pattern of CN addition, H elimination being the main product channel (Decker & Macdonald 2003). In contrast, the recombination channel could be more efficient. A recent theoretical study found that radiative association reactions between radical species can proceed rapidly at low temperatures, such as that of TMC-1 (Tennis et al. 2021). As such, the reaction

$$CN + CH_2CCH \rightarrow CNCH_2CCH + h\nu \tag{20}$$

has been added, with $CNCH_2CCH$ assumed as the sole product and an estimated rate constant of $1.0 \times 10^{-10}\,cm^3\,s^{-1}$, in line with the calculated rate constants for the $CH_3 + CH_3O$ reaction (Tennis et al. 2021). It is likely that the CN-addition, H-elimination channel to form cyano propargyl radicals is in competition; however, we are more interested in determining whether the inclusion of this reaction can reproduce the observed abundance of $CNCH_2CCH$. More experimental and theoretical work is necessary to confirm whether the closed-shell $CNCH_2CCH$ can form in this reaction.

2.5. Grain Chemistry

In addition to the gas-phase chemistry, grain-surface processes, particularly hydrogenation reactions, are likely important in cold interstellar regions. Even at 10 K, light H atoms can move efficiently on grain surfaces, and reactions with activation barriers can occur through quantum mechanical tunneling. Hickson et al. (2016) and Loison et al. (2017) investigated the chemistry of C_3H_n species in cold dense clouds, including hydrogenation of these species on grain surfaces. These authors suggested that such hydrogenation processes can begin with C_3 and proceed all the way to C_3H_8, with the majority of these reactions having no activation barrier. Specifically, the hydrogenation reactions of C_3H_2 isomers to form CH_2CCH,

$$\text{s-H} + \text{s-}l\text{-}C_3H_2 \rightarrow \text{s-}CH_2CCH \tag{21}$$

and

$$\text{s-H} + \text{s-}c\text{-}C_3H_2 \rightarrow \text{s-}CH_2CCH, \tag{22}$$

were found to be barrierless (here "s-" denotes a grain-surface species). Likewise, using quantum chemical calculations, Miller & Klippenstein (2003a) found the hydrogenation of CH_2CCH to CH_3CCH and CH_2CCH_2,

$$\begin{aligned}\text{s-H} + \text{s-}CH_2CCH &\rightarrow \text{s-}CH_3CCH \quad 50\% \\ &\rightarrow \text{s-}CH_2CCH_2 \quad 50\%,\end{aligned} \tag{23}$$

to be barrierless for both C_3H_4 isomers, suggesting that these species can be efficiently formed on grain surfaces. These grain processes of the C_3H_n species were thus incorporated into our network according to Hickson et al. (2016) and Loison et al. (2017), and a full list can be found in Table 8 in Appendix C.

In addition to grain-surface reactions, desorption energies of relevant species were updated according to recent experimental and theoretical studies. Accurate desorption energies for species with efficient grain-surface formation pathways are vital for describing the release of these species into the gas phase. Recent temperature-programmed desorption (TPD) experiments on amorphous water ices reported a value of 4400 K for the desorption energy of CH_3CCH on compact water ice (Behmard et al. 2019). In this study, we used this value for the desorption energy of CH_3CCH in our model and assumed that CH_2CCH_2 has the same desorption energy as that of CH_3CCH. Wakelam et al. (2017) estimated desorption energies for a variety of interstellar species on amorphous solid water using quantum chemical calculations, including the CH_2CCH radical (3300 K). Additionally, Villadsen et al. (2022) predicted binding energies of astrochemically relevant molecules by applying Gaussian process regression to a training set of experimental TPD energies, finding generally good agreement between experiment and predictions. We incorporated their predicted value of 9520 K for the desorption energy of all three C_4H_3N isomers on water surfaces into our model.

2.6. Sensitivity Analysis

In order to gauge the sensitivity of our modeling results to the rate constants of certain reactions, we have performed a sensitivity analysis on a select number of reactions involving CH_2CCH, specifically CH_2CCH reacting with H, C, O, N, CN, OH, and itself. The only formation pathway tested in this manner was Reaction (9), as the rate constants for other formation pathways of CH_2CCH are constrained via low-temperature kinetic measurements or capture theory. For each reaction, the rate constant was multiplied by values ranging from 0.01 to 100, with separate models performed for each modification. Additionally, the removal of each reaction from the network was tested. This technique allows us to determine the effects that different rate constants have on the modeled abundances of interstellar species, which is particularly useful for reactions that lack dedicated low-temperature studies.

However, it is important to note that only one reaction is modified at a time, and thus we do not obtain information about how two reactions may be correlated.

Similarly, we have performed a sensitivity analysis on the effect of the C/O ratio on CH_2CCH, CH_3CCH, and CH_2CCH_2. As stated previously, we assume a C/O ratio of 1.1 in our model in line with previous GOTHAM studies (Xue et al. 2020; Burkhardt et al. 2021b; Loomis et al. 2021; McCarthy et al. 2021; McGuire et al. 2021), as this ratio improves modeling results for a variety of carbon-bearing species, especially the cyanopolyynes. Additionally, Hincelin et al. (2011) and Wakelam et al. (2006) both investigated the effect of C/O ratio on astrochemical models of TMC-1 and found better overall agreement with observations with a larger C/O ratio. However, some models of TMC-1 use a significantly lower C/O ratio of 0.7 (Ruaud et al. 2016; Loison et al. 2017), while other astronomical sources may have different chemical conditions and thus different C/O ratios. We have tested values of the C/O ratio ranging from 0.7 to 1.1 in increments of 0.1 by varying the initial abundance of elemental oxygen.

3. Results

In order to consistently analyze the results of our models, we calculated a best-fit time by minimizing the mean absolute difference between the log observed abundances and the log modeled abundances for species of interest (CH_2CCH, CH_3CCH, $CNCH_2CCH$, CH_3C_3N, and CH_2CCHCN). This gives a best-fit time of 4.739×10^5 yr. 1-cyanonaphthalene ($C_{10}H_7CN$) and 2-cyanonaphthalene ($C_{10}CNH_7$) were excluded from this calculation, as the modeled abundances of these species are still ∼6 orders of magnitude below observations. This value is in agreement with a best-fit time of $\sim 5 \times 10^5$ yr from previous GOTHAM modeling studies (Xue et al. 2020; Loomis et al. 2021).

The modeled column densities of select species at this best-fit time can be seen in Table 3, along with observed values and confidence levels. The latter values were calculated using the method introduced by Garrod et al. (2007) and are a metric of confidence that the best-fit abundance is in agreement with the observed abundance, assuming a lognormal distribution centered on the observed value with a standard deviation of 1. We also calculated the mean confidence level excluding the cyanonaphthalene isomers, as the agreement for these species is very poor and would heavily skew the mean.

In astrochemical models of dark molecular clouds, it can also be assumed that some elements, typically carbon, sulfur, silicon, phosphorus, chlorine, and the metals, begin as cations in their initial state (Ruaud et al. 2016). If the initial elemental abundances as described in Table 1 are kept but the previously mentioned species are assumed to begin as cations, the resulting best-fit abundances increase slightly by factors of 1.21 or less. The relative contributions of production and destruction pathways are affected, such as Reaction (2) becoming less prevalent to the production of CH_2CCH at early times. The similarity in abundances at later times may be due to the efficient conversion of C^+ to C via electron capture and charge transfer.

3.1. C_3H_n Hydrocarbons

In Figure 3, the modeled abundances of CH_2CCH, CH_3CCH, and CH_2CCH_2 are plotted as a function of time, as well as their observed column densities in TMC-1. Gratier et al. (2016) constrained the column density of CH_3CCH as 1.15×10^{14} cm^{-2} based on observations of the TMC-1 cyanopolyyne peak using the Nobeyama 45 m telescope. Agúndez et al. (2021) first detected CH_2CCH at a wavelength of 8 mm with a column density of 8.7×10^{13} cm^{-2} and later used observations at 3 mm to revise the column density to 1.0×10^{14} cm^{-2} (Agúndez et al. 2022). CH_2CCH_2 has not been detected in TMC-1, and thus there is no observed value for this species. The observed column densities, as well as best-fit modeled column densities, can be seen in Table 3. Our updated model gives best-fit abundances of CH_2CCH and CH_2CCH_2 that are ∼60 and ∼29 times lower than observations, respectively. Compared to the model results with the GOTHAM DR1 network, the modeled abundance of CH_2CCH at 4.739×10^5 yr has been increased by a factor of 2.65. The removal of Reactions (11) and (12) resulted in the largest increase to the modeled CH_2CCH abundance, followed by the addition of the neutral–neutral Reactions (9) and (10). The modeled abundance of CH_3CCH at this time has only been increased by a factor of 1.41 compared to the previous model results. The column densities of both CH_2CCH and CH_3CCH are still underpredicted by between 1 and 2 orders of magnitude, although the CH_3CCH abundance is almost within the 1σ confidence interval.

In our updated model, the early-time production of CH_2CCH is dominated by the reaction between atomic carbon and C_2H_4 (Reaction (2)), as shown in Figure 4. Grain-surface hydrogenation of both isomers of C_3H_2 (Reactions (21) and (22)) followed by chemical desorption also contributes significantly to CH_2CCH formation owing to the large abundance of atomic hydrogen and its high mobility on grains. After $\sim 10^4$ yr, the rates of other CH_2CCH formation pathways become sizable owing to the buildup of more complex hydrocarbons. In addition to the aforementioned reactions, the reaction between diatomic carbon and methane (Reaction (10)) and the DRs of $C_5H_5^+$ and $C_3H_4^+$ become significant sources of CH_2CCH around 10^5 yr. Despite a similar rate constant to the DR of $C_5H_5^+$, we find that the DR of $C_3H_5^+$ is unable to efficiently form CH_2CCH at all times. Likewise, the DR of $C_3H_4^+$ has the greatest rate constant of these three reactions but still exhibits a lower rate than the DR of $C_5H_5^+$. This is due to an approximately 10-fold difference in abundance between $C_5H_5^+$ and the $C_3H_n^+$ cations at 10^5 yr. Similarly, the neutral–neutral production pathways of CH_2CCH generally outpace the DR pathways, despite greater rate constants in the latter set of reactions, due to much larger modeled abundances of small neutral hydrocarbons. CH_2CCH is primarily destroyed via reaction with O, C, and N at early times (before 10^5 yr) and via reaction with H at later times (after 3×10^5 yr).

For the first $\sim 10^3$ yr of the model, CH_3CCH is primarily formed by the grain-surface reaction

$$\mathrm{s{-}CH} + \mathrm{s{-}C_2H_3} \rightarrow \mathrm{CH_3CCH}, \tag{24}$$

where energy from reaction exothermicity ejects a portion of the products into the gas phase. At 10^4 yr and later, CH_3CCH is predominantly formed from Reactions (13) and (23). Similarly, Reactions (16) and (23) constitute the main formation pathways of CH_2CCH_2 at all times. Despite the relatively low rate constant, the gas-phase radiative association between H and CH_2CCH is able to efficiently form both C_3H_4 isomers owing to the large abundance of H and increased abundance of

Table 3
Modeled and Observed Column Densities for Select Species

Molecule	Best Fit[a] (cm^{-2})	Observed[b] (cm^{-2})	Confidence Level[c]	References
CH_2CCH	1.67×10^{12}	1.0×10^{14}	0.0757	Agúndez et al. (2022)
CH_3CCH	4.01×10^{12}	1.15×10^{14}	0.145	Gratier et al. (2016)
CH_2CCH_2	5.20×10^{12}	…	…	…
CH_3C_3N	3.36×10^{12}	8.66×10^{11}	0.556	Siebert et al. (2022)
CH_2CCHCN	8.48×10^{11}	2.7×10^{12}	0.615	Marcelino et al. (2021)
$CNCH_2CCH$	2.00×10^{11}	9.2×10^{11}	0.507	McGuire et al. (2020)
$C_{10}H_7CN$	4.44×10^{6}	7.35×10^{11}	1.80×10^{-7}	McGuire et al. (2021)
$C_{10}CNH_7$	4.93×10^{6}	7.05×10^{11}	2.53×10^{-7}	McGuire et al. (2021)
C_6H_5	2.54×10^{11}	…	…	…
Mean confidence level[d]			0.380	

Notes.
[a] Modeled column density at the best-fit time of 4.739×10^5 yr.
[b] Species with no value in this column have not been detected in TMC-1.
[c] Calculated according to Garrod et al. (2007). Species with no value in this column have not been detected in TMC-1.
[d] The cyanonaphthalene isomers ($C_{10}H_7CN$ and $C_{10}CNH_7$) were not included in this calculation.

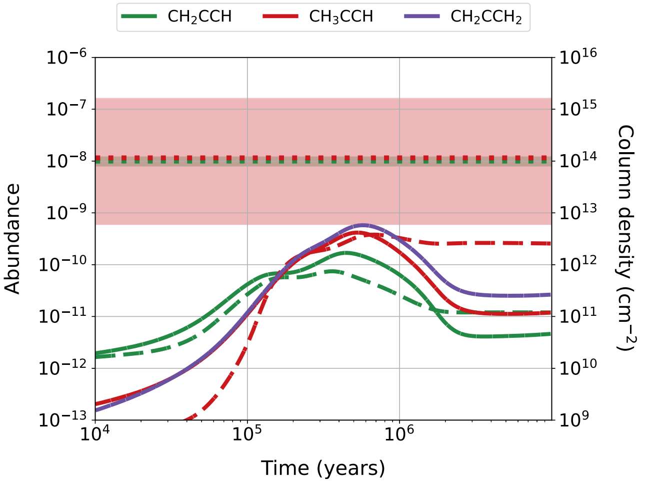

Figure 3. Modeled abundances and column densities of propargyl radical (green), methylacetylene (red), and allene (purple) as a function of time. The dotted lines represent the observed column densities in TMC-1, with the shaded areas signifying an error of 1σ. The dashed lines represent modeled abundances obtained from GOTHAM DR1, and the solid lines are the modeled abundances with the updated model presented in this work.

CH_2CCH. Likewise, the analogous grain-surface hydrogenations are able to form large amounts of C_3H_4 both in the gas phase and on grain surfaces, resulting in high grain-surface abundances for CH_3CCH and CH_2CCH_2. The rates of these reactions as a function of time can be seen in Figures 5 and 6. Destruction of both C_3H_4 isomers occurs mainly through a combination of reaction with C, which dominates before 10^5 yr, and reaction with H_3^+, which dominates shortly after 10^5 yr. Between 10^5 and 10^6 yr, reaction with the CN radical significantly contributes to the destruction of CH_3CCH and CH_2CCH_2. The rates of key destruction mechanisms for CH_2CCH, CH_3CCH, and CH_2CCH_2 as a function of time are displayed in Figure 14 in Appendix D.

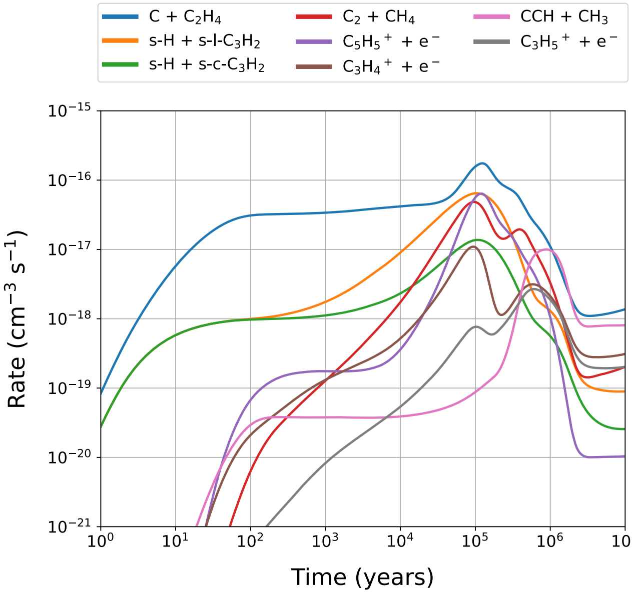

Figure 4. Reaction rates for key CH_2CCH formation pathways as a function of time. Each color represents a different reaction, with the reactants given in the legend ("s-" denotes a grain species). For more information on these reactions, including product channels, refer to Tables 4–8 in the appendices.

3.2. CN-substituted Species

Considering the strong chemical link between pure hydrocarbons and their CN-substituted derivatives in TMC-1, we are interested in how the updated chemical network affects the formation of C_4H_3N isomers. The modeled abundances of these species as a function of time are shown in Figure 7. The best-fit column densities of these species as calculated by the model are listed in Table 3, along with their observed column densities. The best-fit column density of CH_2CCHCN is predicted particularly well by our model to within a factor of ∼3.2, whereas the best-fit column density for $CNCH_2CCH$ is only a factor of ∼4.4 lower than the observed value. Finally, our model overpredicts the column density of CH_3C_3N by a factor of ∼3.8. Compared to the GOTHAM DR1 model, the CH_3C_3N abundance does not change significantly despite the incorporation of a new formation route in Reaction (18), suggesting that the contribution from this reaction is only minor.

The decrease in the modeled abundance of $CNCH_2CCH$ stems from the change in its formation pathways, particularly

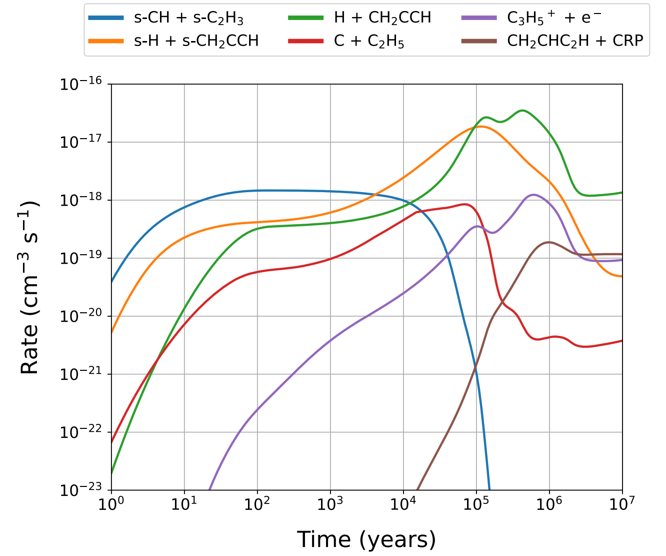

Figure 5. Reaction rates for key CH_3CCH formation pathways as a function of time. Each color represents a different reaction, with the reactants given in the legend ("s-" denotes a grain species, and "CRP" denotes a cosmic-ray-induced photon). For more information on these reactions, including product channels, refer to Tables 4–8 in the appendices.

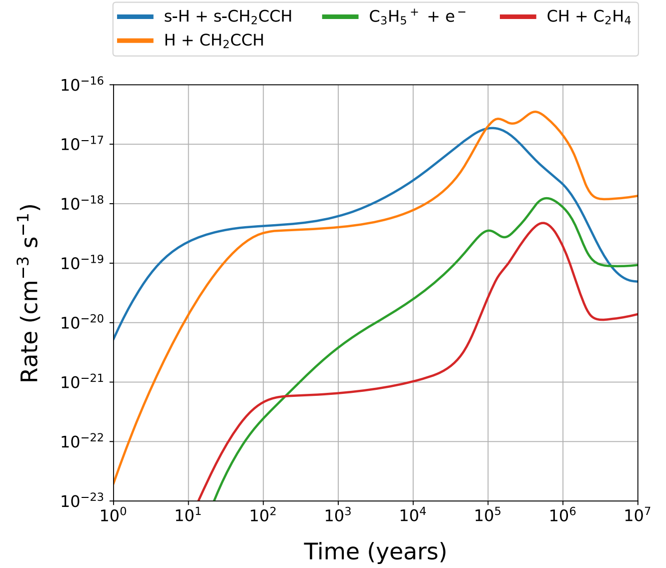

Figure 6. Reaction rates for key CH_2CCH_2 formation pathways as a function of time. Each color represents a different reaction, with the reactants given in the legend ("s-" denotes a grain species). For more information on these reactions, including product channels, refer to Tables 4–8 in the appendices.

the removal of Reaction (18) as a formation route to this species. The addition of new production routes in Reactions (20) and (19) is able to nearly reproduce the GOTHAM DR1 abundance, despite $CNCH_2CCH$ being only a minor product of the latter reaction. Before 3×10^5 yr, the formation of $CNCH_2CCH$ is dominated by Reaction (20), and following this time, Reaction (19) becomes the dominant formation pathway. As mentioned in Section 2, we tested models with alternate products for ion–neutral reactions of $CNCH_2CCH$ and CH_2CCHCN to determine their effects on the abundances of species considered here. When alternate product channels were used, the peak abundance of the directly affected species, CH_2CCH, decreased by a factor less than 1.15. Likewise, the peak abundances of the C_3H_4 and C_4H_3N isomers changed by factors of less than 1.2. Considering the almost negligible differences in results, the products of these ion–neutral reactions do not seem to significantly affect the species of interest.

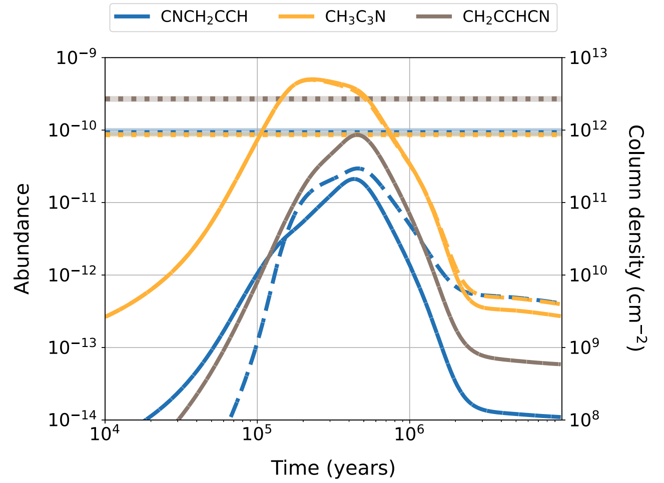

Figure 7. Modeled abundances and column densities of propargyl cyanide (blue), methylcyanoacetylene (yellow), and cyanoallene (brown) as a function of time. The dotted lines represent the observed column densities in TMC-1, with the shaded areas signifying an error of 1σ. The dashed lines represent modeled abundances from GOTHAM DR1, and the solid lines are the modeled abundances with the updated model presented in this work.

3.3. Aromatic Species

In addition to the previously mentioned species, we also examined C_6H_5 and the two cyanonaphthalene isomers to determine the effect of the propargyl recombination reaction on the formation of these species. These abundances are plotted as a function of time in Figure 8, and the best-fit modeled abundances can be seen in Table 3. The astrochemical model still severely underpredicts the column densities of 1- and 2-cyanonaphthalene ($C_{10}H_7CN$, $C_{10}CNH_7$), although the modeled abundances of the cyanonaphthalenes have been increased by about a factor of 1.7 at the best-fit time for both isomers. The two $C_{10}H_7CN$ isomers are primarily produced from reaction between naphthalene ($C_{10}H_8$) and CN, while the main production pathway for $C_{10}H_8$ is the reaction between C_6H_5 and CH_2CHC_2H. The reaction of CN with benzene to form C_6H_5CN is barrierless and efficient at low temperatures, and the analogous reaction with $C_{10}H_8$ to form $C_{10}H_7CN$ is expected to be as well (Cooke et al. 2020; McGuire et al. 2021). Thus, it is the formation of $C_{10}H_8$ that limits production of $C_{10}H_7CN$. Our addition of CH_2CCH_2 as a species and its reaction with CH to form CH_2CHC_2H lead to an increase in $C_{10}H_8$ abundance and an increase in $C_{10}H_7CN$ abundance as a result.

The modeled abundance of C_6H_5 has not been changed by the addition of CH_2CCH recombination (Reaction (14)), except for at early times. At these times a significant increase in C_6H_5 abundance is observed, but this difference is made up for by a time of 100 yr. To understand why, we must look at the other production mechanisms for C_6H_5 included in our network. These are dissociation of benzene via cosmic-ray-induced photons or external photons and hydrogen abstraction from benzene via OH and H. Activation barriers to hydrogen abstraction and a large visual extinction make dissociation by

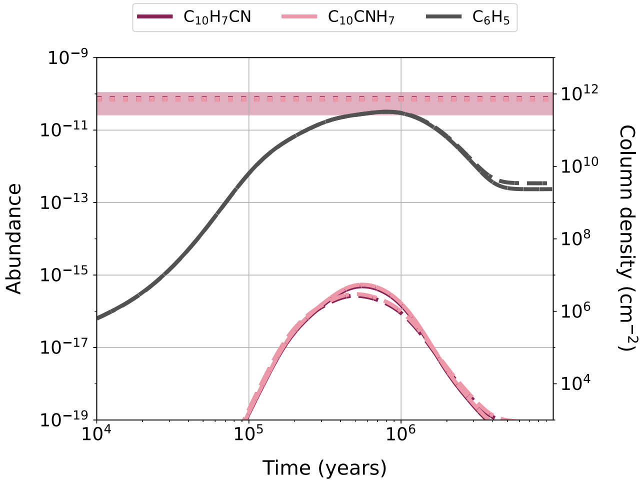

Figure 8. Modeled abundances and column densities of 1-cyanonaphthalene ($C_{10}H_7CN$; maroon), 2-cyanonaphthalene ($C_{10}CNH_7$; pink), and C_6H_5 (gray) as a function of time. The dotted lines represent the observed column densities in TMC-1, with the shaded areas signifying an error of 1σ. The dashed lines represent modeled abundances from GOTHAM DR1, and the solid lines are the modeled abundances with the updated model presented in this work. As the formation pathways and observed TMC-1 abundances of the two cyanonaphthalene isomers are very similar, the plotted curves for one isomer are overlapping with those of the other.

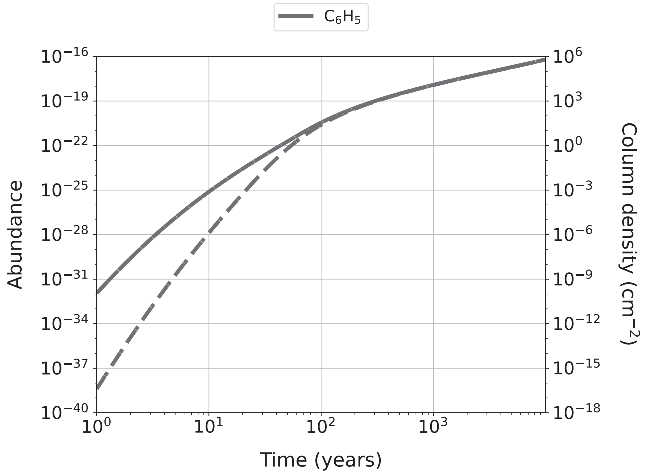

Figure 9. Modeled abundances and column densities of the phenyl radical from 1 to 10^4 yr. The dashed line represents modeled abundances from GOTHAM DR1, and the solid line represents the modeled abundances of the updated model presented in this work.

cosmic-ray-induced photons the major mechanism. At early times, the modeled benzene abundance is over 10 orders of magnitude lower than the modeled propargyl abundance. However, the benzene abundance quickly increases, and this difference becomes only 6 orders of magnitude at 50 yr. At this point, the unimolecular decomposition becomes fast enough to outpace the bimolecular recombination of CH_2CCH. Although CH_2CCH abundance has been increased at most times, the resulting rate is not large enough to exceed the rate for C_6H_6 dissociation. This can be seen in Figure 9, where the modeled abundance of the phenyl radical is significantly increased in our new model compared to GOTHAM DR1 at early times but the GOTHAM DR1 abundance makes up the difference by approximately 100 yr.

3.4. Sensitivity Studies of Key Reactions and C/O Ratio

In addition to the astrochemical modeling performed using the updated chemical network, we have also performed sensitivity studies on this chemical network to investigate the importance of several reactions to the chemistry of CH_2CCH. The results of these studies on Reaction (20) can be seen in Figure 10. When the rate constant for this reaction is increased by 1 order of magnitude to a value of 1.0×10^{-9} cm^3 s^{-1}, the best-fit abundance of $CNCH_2CCH$ increases by a factor of almost 5, essentially reproducing the observed value. The best-fit abundance continues to increase beyond the observed value as the rate constant is further raised. If this reaction is removed from the network entirely, the best-fit abundance of $CNCH_2CCH$ only decreases by a factor of 1.7 compared to the presented network. In contrast, there is no noticeable change in the modeled abundance of CH_2CCH, even when this rate constant is increased by 2 orders of magnitude or removed from the network entirely.

This procedure has been repeated for the reactions of CH_2CCH with C, H, N, O, OH, and CH_2CCH, as well as for the reaction $CCH + CH_3 \rightarrow CH_2CCH + H$. The modeled abundances of CH_2CCH, CH_3CCH, and CH_2CCH_2 for different rate constants of the $CH_2CCH + H$ reaction are shown in Figures 11–13. Both increases and decreases to this rate constant are shown to have large effects on modeled abundances of all three species, with the most noticeable variation in CH_2CCH abundance. Figures 15 and 16 in Appendix E display the modeled abundances of CH_2CCH in response to variations in the remaining rate constants. For the reactions of CH_2CCH with itself and OH, none of the tested changes significantly alter the modeled abundance of CH_2CCH. Furthermore, the best-fit abundance of C_6H_5 only changes slightly when the rate constant of the propargyl recombination is modified. Lowering the rate constant or removing the reactions of CH_2CCH with C, N, and O also does not change the modeled abundance of CH_2CCH; however, increasing the rate constants of these reactions does significantly lower the best-fit abundance. Likewise, removing Reaction (9) ($CCH + CH_3$) does not have a significant effect on CH_2CCH abundance, while increasing this rate leads to a slight increase in CH_2CCH abundance at a later time.

The results of our C/O sensitivity tests can be seen in Figure 17 in Appendix E. As the C/O ratio is lowered from 1.1 to 0.7, the late-time abundances ($\sim 5 \times 10^5$ yr) of CH_2CCH, CH_3CCH, and CH_2CCH_2 significantly decrease, with smaller decreases in early-time ($\sim$(1–2) $\times 10^5$ yr) abundances. In particular, the abundance of CH_2CCH at our best-fit time decreases by a factor of 22 when the C/O ratio is lowered from 1.1 to 0.7. The maximum modeled column density of CH_2CCH using a C/O ratio of 0.7 is almost a factor of 7 lower than the best-fit abundance using a C/O ratio of 1.1. Likewise, the mean confidence level of CH_2CCH, CH_3CCH, CH_2CCH_2, and the C_4H_3N isomers decreases from 0.385 to 0.174 when the C/O ratio is changed from 1.1 to 0.7. These results indicate that CH_2CCH and its closed-shell relatives are somewhat sensitive to the C/O ratio, with a larger value favoring the formation of these species.

4. Discussion

4.1. Dark Molecular Cloud Chemistry of C_3H_3 and C_3H_4 Species

As noted by Agúndez et al. (2021) in their initial detection, CH_2CCH is one of the most abundant radicals detected in TMC-1, with a derived column density only slightly below that

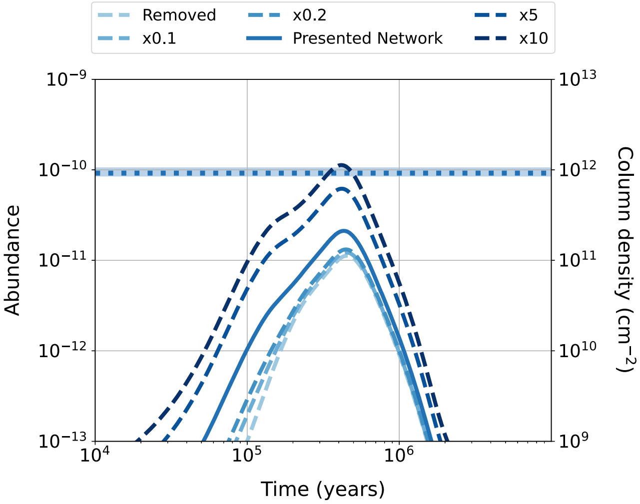

Figure 10. Modeled abundances and column densities of $CNCH_2CCH$ for different values of the CN + CH_2CCH rate constant. The dashed lines are networks where this rate constant has been modified by the factors in the legend. The base network (presented in this paper) is shown for comparison as a solid line, as well as a network where this reaction is removed entirely. The color gradient corresponds with the magnitude of the factor of change. As with the previous figures, a dotted horizontal line is plotted representing the observed abundance of $CNCH_2CCH$ in TMC-1, with the shaded region signifying an error of 1σ.

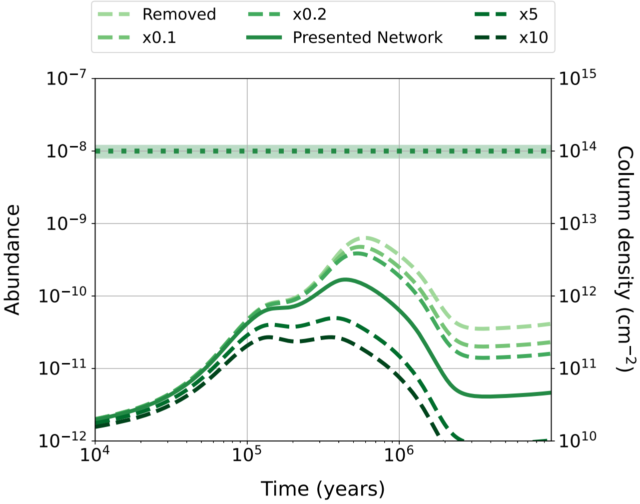

Figure 11. Modeled abundances and column densities of CH_2CCH for different values of the $CH_2CCH + H$ rate constant. The dashed lines are networks where this rate constant has been modified by the factors in the legend. The base network (presented in this paper) is shown for comparison as a solid line, as well as a network where this reaction is removed entirely. The color gradient corresponds with the magnitude of the factor of change. The dotted line represents the observed column density in TMC-1, with the shaded area signifying an error of 1σ.

of the closed-shell CH_3CCH. As the authors remark, this radical is an example of a resonance-stabilized radical, and as such the delocalization of the unpaired electron is expected to lower its reactivity compared to radicals without resonance. In addition to the detection, the authors use astrochemical modeling to investigate the major formation and destruction mechanisms of CH_2CCH and its closed-shell relatives. They achieve a peak modeled abundance of $\sim 1 \times 10^{-10}$ with respect to H_2, similar to our model, but at an earlier time of 2×10^5 yr. They also obtain much larger modeled abundances of CH_3CCH

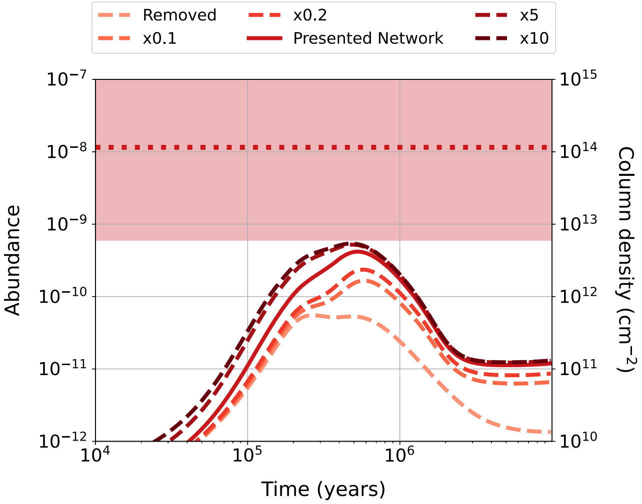

Figure 12. Modeled abundances and column densities of CH_3CCH for different values of the $CH_2CCH + H$ rate constant. The dashed lines are networks where this rate constant has been modified by the factors in the legend. The base network (presented in this paper) is shown for comparison as a solid line, as well as a network where this reaction is removed entirely. The color gradient corresponds with the magnitude of the factor of change. The dotted line represents the observed column density in TMC-1, with the shaded area signifying an error of 1σ.

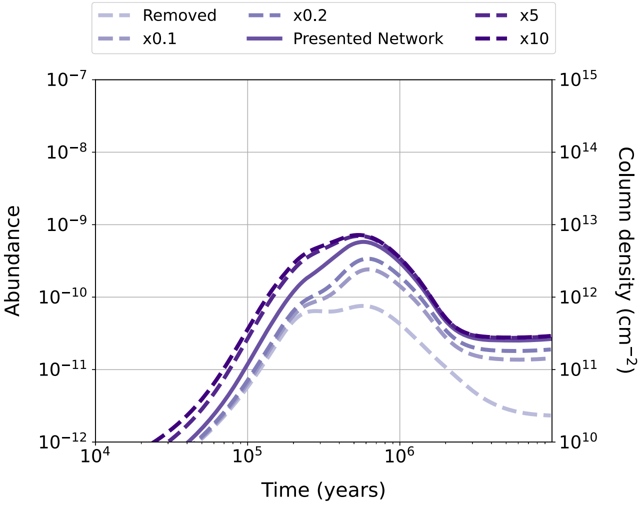

Figure 13. Modeled abundances and column densities of CH_2CCH_2 for different values of the $CH_2CCH + H$ rate constant. The dashed lines are networks where this rate constant has been modified by the factors in the legend. The base network (presented in this paper) is shown for comparison as a solid line, as well as a network where this reaction is removed entirely. The color gradient corresponds with the magnitude of the factor of change.

and CH_2CCH_2 on the order of 10^{-8} at a time of $\sim 5 \times 10^5$ yr, close to the TMC-1 observed value for CH_3CCH.

In terms of production pathways, our models agree that Reaction (2) is the dominant pathway toward forming CH_2CCH. The kinetics of this reaction were measured twice from 295 to 15 K by Chastaing et al. (1999, 2001) using the CRESU technique and two different product detection techniques. In both cases, the data were fit via a nonlinear least-squares fit to a modified Arrhenius form, yielding a temperature-dependent rate constant of $k(T) = 3.1 \times 10^{-10} (T/298\ \mathrm{K})^{-0.07}\ \mathrm{cm}^3\ \mathrm{s}^{-1}$ from the first set of measurements and $k(T) = 3.0 \pm 0.4 \times 10^{-10}$ $(T/298\ \mathrm{K})^{-0.11 \pm 0.07}\ \mathrm{cm}^{31}\ \mathrm{s}^{-1}$ from a fit combining both sets of measurements. The strong agreement between the two sets of measurements and relatively low errors in fit parameters and individual rate constant measurements suggest that this reaction is fast at 10 K with a rate constant near 4×10^{-10} cm^3 s^{-1}. The KIDA database and our model currently use the temperature-dependent fit from Chastaing et al. (1999), while Agúndez et al. (2021) use a slightly smaller, temperature-independent value of 3.1×10^{-10} cm^3 s^{-1}. A number of experimental and theoretical studies (Bergeat & Loison 2001; Le et al. 2001; Geppert et al. 2003; Chin et al. 2012; Mandal et al. 2018) indicate that $CH_2CCH + H$ is the only major product channel, resulting from more than 90% of reactions.

However, Agúndez et al. (2021) also observe that CH_3CCH and CH_2CCH_2 are primarily formed from the DRs of $C_3H_n^+$ cations. In our model, the DR of $C_3H_5^+$ is inefficient compared to gas-phase and grain-surface hydrogenations of CH_2CCH, and $C_3H_n^+$ cations larger than $C_3H_5^+$ are not included in the network. This suggests significant differences in chemical networks, particularly regarding the chemistry of C_3H_n species. Inclusion of larger neutral and cationic C_3H_n species and a thorough investigation of their formation paths in cold molecular clouds would benefit modeling of CH_2CCH and the C_3H_4 isomers.

The model of Agúndez et al. (2021) agrees with our model that the major destruction mechanisms of CH_2CCH are with atoms such as C, N, and O, although they do not consider the radiative association of CH_2CCH with H. The authors propose that CH_2CCH could be reproduced by the model if reactions with O and N atoms are removed, or alternatively if the initial C/O ratio is above 1. Despite an initial C/O ratio of 1.1, we obtain a similar maximum abundance of CH_2CCH to their initial model. Additionally, our sensitivity analysis of CH_2CCH reactions shows that the maximum abundance of CH_2CCH is not significantly affected by the removal of any individual reaction except for $CH_2CCH + H$. This barrierless reaction is estimated to be fairly efficient at low temperature based on a semiempirical approach involving reaction exothermicity and molecule size; however, there is significant uncertainty in the rate constant (Hébrard et al. 2013). We find that CH_2CCH, CH_3CCH, and CH_2CCH_2 abundances are all sensitive to this rate constant, as this reaction is a major destruction mechanism for the first species and a major production mechanism for the other two. A decrease in the rate constant would lead to a significantly larger modeled abundance for CH_2CCH, which could then be compounded by removal of the $CH_2CCH + O$ and $CH_2CCH + N$ reactions. However, such a scenario could result in significant decreases to the modeled abundances of CH_3CCH and CH_2CCH_2. Potential energy surface calculations on the $CH_2CCH + O$ and $CH_2CCH + N$ reactions, as well as an experimental measurement of the $CH_2CCH + H$ radiative association rate constant and branching ratios, would significantly improve our understanding of propargyl radical chemistry in cold molecular clouds.

Neither our model nor the model of Agúndez et al. (2021) considers the reaction between CCH and CH_3 to be a major formation reaction for CH_2CCH. In our model, the rate for this reaction is slow compared to many other CH_2CCH production mechanisms at most times. It is not until $\sim 10^6$ yr, after the expected age of TMC-1, that this rate becomes large enough for the reaction to be significant to CH_2CCH formation. Both reactants experience significant increases in modeled abundance, over an order of magnitude for CH_3 and slightly less for CCH, from 10^5 to 10^6 yr. As the major destruction pathways for these species are with C, N, and O atoms, these increases in abundance may be due to the drop in neutral atom abundances during this time period. The rate constant for this reaction was estimated to be 1×10^{-10} cm^3 s^{-1} as an approximate value for a radical–radical association followed by H elimination, but without any experimental or theoretical studies there is significant uncertainty in this value. Our sensitivity analysis of the rate constant for this reaction reveals that an increase in this rate constant could result in a moderate increase to modeled CH_2CCH abundance, but not until after 6×10^5 yr. Decreasing this rate constant or removing this reaction only leads to a slight decrease in CH_2CCH abundance after this time and a negligible decrease before then.

4.2. C_4H_3N Isomers and CH_2CCH_2 Abundance Constraint

In cold molecular clouds, the CN radical is thought to react efficiently with many unsaturated hydrocarbons via a CN-addition H-elimination pathway (Balucani et al. 2000; Carty et al. 2001; Cooke et al. 2020). The ability of our model to reproduce the observed column densities of CH_2CCHCN and $CNCH_2CCH$ within a factor of 5 further demonstrates the importance of this mechanism in forming interstellar CN derivatives. The column density of CH_3C_3N is also reproduced by our model within a factor of 5; however, the major mechanism for this species is the DR of $H_3C_4NH^+$. In addition to a 10% branching ratio from Reaction (19), we assumed a radiative association reaction between CH_2CCH and CN to produce $CNCH_2CCH$ with a rate constant of 1.0×10^{-10} cm^3 s^{-1}. Our sensitivity analysis of this reaction reveals that an order-of-magnitude increase in this rate constant could reproduce the observed $CNCH_2CCH$ abundance; however, such a large rate constant is unreasonable for an association reaction between two neutral species. Conversely, lowering this rate constant or removing the reaction entirely only slightly lowers the best-fit abundance, resulting in a value still within an order of magnitude compared to observations. As the major formation route to $CNCH_2CCH$ and CH_2CCHCN is through CH_2CCH_2, it is possible that a deficiency in modeled CH_2CCH_2 is responsible for the deficiencies in these two C_4H_3N isomers.

Quan & Herbst (2007) have performed astrochemical modeling on CH_2CCHCN and CH_3C_3N, testing the effects of different CH_3CCH/C_3H_4 ratios on abundances at 10^5 yr. Using branching ratios of 50/50 CH_2CCHCN/CH_3C_3N for $CN + CH_3CCH$ and 90/10 $CH_2CCHCN/CNCH_2CCH$ for $CN + CH_2CCH_2$, the authors find the best agreement with observations when the CH_3CCH abundance is 35% of the total C_3H_4 abundance. More recent branching ratio measurements for $CN + CH_3CCH$ suggest that CH_2CCHCN is not formed significantly at low temperature (Abeysekera et al. 2015), and the detection of $CNCH_2CCH$ allows for the inclusion of the third C_3H_4N isomer in the analysis. More recently, Marcelino et al. (2021) examined all three C_4H_3N isomers using astrochemical modeling, testing both sets of experimental branching ratios for $CN + CH_3CCH$. The authors obtain very similar results to our own model, finding good agreement with observations for all three species. As in our study, they find that the DR of $H_3C_4NH^+$ is mainly responsible for the formation of CH_3C_3N. They also find that the choice in branching ratios for $CN + CH_3CCH$ does not notably affect the resulting modeled abundances.

Since CH_2CCH_2 is a symmetric hydrocarbon and does not possess a permanent dipole moment, it is not possible to detect this species via radio astronomy. However, a rough estimate of its TMC-1 abundance can be made using our modeled CH/CN ratio and the observed abundance of CH_2CCHCN. Taking the ratio of CH_2CCH_2 to CH_2CCHCN at our best-fit time, 6.1, and multiplying it by the observed column density of CH_2CCHCN, we obtain an extrapolated CH_2CCH_2 column density of 1.64×10^{13} cm^{-2}. This value is almost an order of magnitude lower than the observed column density of CH_3CCH and would suggest a difference in interstellar chemistry between these species that is not present in our model, although it is within the 1σ uncertainty of the observed CH_3CCH column density. It is important to note that modeled CH/CN ratios are sensitive to the model parameters used, such as the rate constant for the CN-addition H-elimination pathway (Sita et al. 2022), as well as the time of choice. Although the $CN + CH_2CCH_2$ rate constant has been measured at low temperature (Carty et al. 2001), the branching ratios have not. Additionally, CH/CN ratios could be significantly different in other interstellar regions with different physical and chemical conditions. Thus, this method of column density approximation is only a rough estimate based on certain modeling parameters and our time of best fit. A detailed analysis of CH/CN ratios in TMC-1, as well as a more constrained column density for CH_3CCH, would be beneficial toward understanding the relationship between these two isomers and their CN-substituted derivatives.

4.3. Implications for PAH Formation

C_6H_5 is an aromatic resonance-stabilized radical and a key precursor to formation of PAHs in cold molecular clouds. The Hydrogen Abstraction−Vinylacetylene Addition (HAVA) mechanism, which begins with the addition of C_6H_5 to vinylacetylene followed by rearrangement and hydrogen loss, is one viable low-temperature formation pathway to $C_{10}H_8$ and larger PAHs (Parker et al. 2012; Kaiser & Hansen 2021). This mechanism is the major generator of $C_{10}H_8$ in our chemical network. Likewise, indene can be formed via reactions of C_6H_5 with small hydrocarbons, although these reactions are so far limited to high temperature (Doddipatla et al. 2021; Kaiser & Hansen 2021). An understanding of the production of the C_6H_5 in TMC-1 is critical for describing the formation of $C_{10}H_8$, indene, and other PAHs in cold molecular clouds. A major motivation of modeling CH_2CCH was to assess its role as an interstellar aromatic precursor; however, addition of the CH_2CCH recombination reaction resulted in no significant change to C_6H_5 abundance after 100 yr. Based on the sensitivity analysis of this reaction, increasing this rate constant by an order of magnitude does not appreciably change the best-fit abundance of C_6H_5, nor would this increase agree with the temperature dependence calculated by Georgievskii et al. (2007). Thus, the abundance of CH_2CCH appears to be the limiting factor. As the CH_2CCH recombination reaction is second order in CH_2CCH abundance, a deficiency in CH_2CCH abundance by almost 2 orders of magnitude would lead to a recombination rate that is lowered by almost 4 orders of magnitude. Continuing to improve our understanding of propargyl radical chemistry is necessary to assess the role of this species in PAH formation. Furthermore, a detection of C_6H_5 in TMC-1 and a derived column density would allow us to better gauge our knowledge of interstellar aromatic chemistry.

Additional reactions of resonance-stabilized radicals, including CH_2CCH, may be important to the formation of aromatic species in dark molecular clouds. In combustion flames, CH_2CCH is thought to react with allyl radicals (C_3H_5) to form fulvene ($C_5H_4CH_2$),

$$CH_2CCH + C_3H_5 \rightarrow C_4H_4CH_2 + H + H, \tag{25}$$

followed by isomerization to benzene (Miller et al. 2010). The authors calculated the potential energy surface for this system and found it to be a barrierless addition with two exothermic, bimolecular exit channels corresponding to two isomers of the hydrofulvenyl radical ($C_5H_5CH_2$). They also predicted the rate constant for this reaction to be on the order of 10^{-10} cm^{-3} s^{-1} at low temperature, independent of the pressure. Moreover, calculations on the $C_6H_5 + CH_2CCH$ potential energy surface have been performed by Morozov & Mebel (2020), resulting in two barrierless sites for addition of CH_2CCH to C_6H_5. The addition of CH_2CCH via its CH_2 terminal yields 3-phenyl-1-propyne ($C_6H_5CH_2CCH$), which can decompose via H loss directly to form C_6H_5CHCCH or after isomerization to form the indenyl radical (C_9H_7)

$$\begin{aligned} CH_2CCH + C_6H_5 &\rightarrow C_6H_5CH_2CCH \\ C_6H_5CH_2CCH &\rightarrow C_6H_5CHCCH + H \\ &\rightarrow C_9H_7 + H. \end{aligned} \tag{26}$$

Addition of CH_2CCH via its CH terminal results in phenylallene ($C_6H_5CHCCH_2$), which can also isomerize to C_9H_7 or immediately decompose to form two monocyclic H-loss products

$$\begin{aligned} CH_2CCH + C_6H_5 &\rightarrow C_6H_5CHCCH_2 \\ C_6H_5CHCCH_2 &\rightarrow C_6H_5CCCH_2 + H \\ &\rightarrow C_6H_5CCCH_2 + H \\ &\rightarrow C_6H_5CHCCH + H. \end{aligned} \tag{27}$$

The mixture of these products is not known at temperatures relevant to dark molecular clouds, nor is the rate constant, but this reaction presents a promising formation route for monocyclic and bicyclic aromatic species. The radical–radical reaction between CH_2CCH and the benzyl radical (C_7H_7) may be yet another key process to PAH formation in dark molecular clouds. A recent theoretical study (Krasnoukhov et al. 2022) on the $C_7H_7 + CH_2CCH$ potential energy surface has shown that CH_2CCH can add to the $-CH_2$ group of C_7H_7 without barrier, leading to a variety of exothermic bimolecular exit channels. Possible products consist of bicyclic aromatic species such as methyleneindanyl radicals ($C_9H_7CH_2$), methyleneindenes ($C_9H_6CH_2$), H-naphthalenyl ($C_{10}H_9$), and naphthalene ($C_{10}H_8$). In the high-temperature environments of asymptotic branch stars, C_7H_7 is formed from H abstraction of toluene (C_7H_8), which itself is formed from benzene or C_6H_5 (Krasnoukhov et al. 2022). It is currently not known whether C_7H_8 or C_7H_7 can be formed efficiently under dark molecular cloud conditions. Likewise, computational studies of fulvenallene (C_7H_6) and the corresponding fulvenallenyl radical (C_7H_5) in combustion environments suggest that the C_7H_5 radical can be formed from H abstraction of C_7H_6 and further react to form PAHs, such as naphthalene via reaction with CH_2CCH (da Silva & Bozzelli 2009). Fulvenallene has been detected recently in TMC-1, with the reaction between cyclopentadiene and the ethynyl radical proposed as a possible formation pathway (Cernicharo et al. 2022). Further investigation of these larger resonance-stabilized radicals under dark molecular cloud conditions will greatly benefit the understanding of PAH formation in these regions.

5. Conclusions

We performed astrochemical modeling on the propargyl radical, CH_2CCH, and related species using the `NAUTILUS` code and an updated chemical network. We also incorporate two new species, CH_2CCH_2 and CH_2CCHCN, into the network. We find that the predicted abundance of CH_2CCH is improved by about an order of magnitude, but it is still almost 2 orders of magnitude below the observed value. The C_4H_3N isomers are found to be formed primarily from CH_3CCH, CH_2CCH_2, and CH_2CCH. We obtain predicted abundances for these C_4H_3N isomers within 1 order of magnitude of the observed values, suggesting that our chemical model is able to account for the major formation mechanisms of these species. We do not observe any significant improvements for aromatic species, but CH_2CCH remains a potential precursor to aromatic species in dark molecular clouds. Further studies of interstellar C_3H_n and resonance-stabilized radical chemistry under conditions relevant to dark molecular clouds would provide key information for improved astrochemical modeling of the species presented here.

Acknowledgments

We thank V. Wakelam for use of the `NAUTILUS` v1.1 code. B.A.M. and C.X. gratefully acknowledge support of National Science Foundation grant AST-2205126. A.N.B. thanks Dr. Troy Van Voorhis for his advice and thoughtful discussions regarding modeling of chemical kinetics.

Appendix A
Dissociative Recombination Reactions

In Table 4, new and updated rate coefficients (k) are listed for the DR of $C_3H_4^+$ and $C_3H_5^+$, two reactions that produce CH_2CCH. As stated in Section 2.1.1 of the main text, the branching ratios for $C_3H_4^+$ were experimentally determined by Geppert et al. (2004), while the branching ratios for $C_3H_5^+$ were estimated by Loison et al. (2017) based on experimental results by Angelova et al. (2004) and photodissociation studies of the C_3H_4 isomers. As the exact branching ratios for the latter species are estimates, there is still significant uncertainty regarding these values. The reactions with a listed rate constant of 0 are ones that have been removed from the chemical network.

Table 4
Related DR Reactions

Reactions	α ($cm^3\ s^{-1}$)	β	γ (K)	k (10 K) ($cm^3\ s^{-1}$)[a]	References
$C_3H_4^+ + e^- \rightarrow H + CH_2CCH$	6.00×10^{-7}	−0.70	0	6.49×10^{-6}	Branching ratios and rate constant from Loison et al. (2017),
$C_3H_4^+ + e^- \rightarrow CCH + CH_3$	1.00×10^{-8}	−0.70	0	1.08×10^{-7}	based on branching ratios from Geppert et al. (2004) and a
$C_3H_4^+ + e^- \rightarrow CH_2 + C_2H_2$	4.00×10^{-8}	−0.70	0	4.33×10^{-7}	lower rate constant in line with other CRYRING
$C_3H_4^+ + e^- \rightarrow H + H + c\text{-}C_3H_2$	1.00×10^{-8}	−0.70	0	1.08×10^{-7}	measurements (Larsson et al. 2005; Fournier et al. 2013)
$C_3H_4^+ + e^- \rightarrow H + H + l\text{-}C_3H_2$	1.00×10^{-8}	−0.70	0	1.08×10^{-7}	
$C_3H_4^+ + e^- \rightarrow H_2 + l\text{-}C_3H_2$	0	0	0	0	
$C_3H_4^+ + e^- \rightarrow H_2 + c\text{-}C_3H_2$	0	0	0	0	
$C_3H_4^+ + e^- \rightarrow CH + C_2H_3$	0	0	0	0	
$C_3H_5^+ + e^- \rightarrow H_2 + CH_2CCH$	4.20×10^{-8}	−0.70	0	4.54×10^{-7}	Branching ratios and rate constant from Loison et al. (2017),
$C_3H_5^+ + e^- \rightarrow H + CH_3CCH$	7.00×10^{-8}	−0.70	0	7.57×10^{-7}	assuming same overall rate as $C_3H_4^+$ DR; 87% C_3 channel
$C_3H_5^+ + e^- \rightarrow H + H + CH_2CCH$	1.10×10^{-7}	−0.70	0	1.19×10^{-6}	and 13% C_2 + C channel from Angelova et al. (2004),
$C_3H_5^+ + e^- \rightarrow H + H_2 + c\text{-}C_3H_2$	1.00×10^{-7}	−0.70	0	1.08×10^{-6}	with exact branching ratios estimated from C_3H_4
$C_3H_5^+ + e^- \rightarrow H + H_2 + l\text{-}C_3H_2$	5.00×10^{-8}	−0.70	0	5.41×10^{-7}	photodissociation studies
$C_3H_5^+ + e^- \rightarrow C_2H_2 + CH_3$	4.70×10^{-8}	−0.70	0	5.08×10^{-7}	
$C_3H_5^+ + e^- \rightarrow H + CH_2 + C_2H_2$	4.70×10^{-8}	−0.70	0	5.08×10^{-7}	
$C_3H_5^+ + e^- \rightarrow H + CH_2CCH_2$	1.10×10^{-7}	−0.70	0	1.19×10^{-6}	

Note.

[a] The rate constants of DR reactions are computed using the modified Arrhenius equation: $k = \alpha(T/300)^{\beta}e^{-\gamma/T}$, where α is a temperature-independent prefactor, β is a unitless temperature dependence parameter, and γ is the activation energy in K.

Appendix B
Ion–Molecule Reactions

Table 5 lists the updated rate coefficients (*k*) for the reactions of CH_2CCH with interstellar cations, while Table 6 lists those of four species chemically related to CH_2CCH with abundant interstellar cations. The rate coefficients were calculated using the Su–Chesnavich equations and the dipole and polarizability values from Table 2. In the case of multiple product channels for one reaction, the branching ratios are assumed to be an even split among all product channels. In actuality this is likely not the case; however, these branching ratios do not have a notable effect on our model, as these reactions primarily act as destruction mechanisms.

Table 5
Ion–Molecule Reactions of Propargyl Radical

Reactions	α	β	γ (K)	k (10 K) ($cm^3\ s^{-1}$)	Formula[a]
$CH_2CCH + H^+ \rightarrow H_2 + c\text{-}C_3H_2^+$	0.25	5.570×10^{-9}	0.2211	1.66×10^{-9}	5
$CH_2CCH + H^+ \rightarrow H_2 + l\text{-}C_3H_2^+$	0.25	5.570×10^{-9}	0.2211	1.66×10^{-9}	5
$CH_2CCH + H^+ \rightarrow H + c\text{-}C_3H_3^+$	0.25	5.570×10^{-9}	0.2211	1.66×10^{-9}	5
$CH_2CCH + H^+ \rightarrow H + l\text{-}C_3H_3^+$	0.25	5.570×10^{-9}	0.2211	1.66×10^{-9}	5
$CH_2CCH + He^+ \rightarrow H + He + H_2 + C_3^+$	0.25	2.888×10^{-9}	0.2211	8.64×10^{-10}	5
$CH_2CCH + He^+ \rightarrow He + H_2 + C_3H^+$	0.25	2.888×10^{-9}	0.2211	8.64×10^{-10}	5
$CH_2CCH + He^+ \rightarrow H + He + c\text{-}C_3H_2^+$	0.25	2.888×10^{-9}	0.2211	8.64×10^{-10}	5
$CH_2CCH + He^+ \rightarrow H + He + l\text{-}C_3H_2^+$	0.25	2.888×10^{-9}	0.2211	8.64×10^{-10}	5
$CH_2CCH + C^+ \rightarrow H_2 + C_4H^+$	0.25	1.816×10^{-9}	0.2211	5.43×10^{-10}	5
$CH_2CCH + C^+ \rightarrow C + l\text{-}C_3H_3^+$	0.25	1.816×10^{-9}	0.2211	5.43×10^{-10}	5
$CH_2CCH + C + \rightarrow H + C_4H_2^+$	0.25	1.816×10^{-9}	0.2211	5.43×10^{-10}	5
$CH_2CCH + C^+ \rightarrow C + c\text{-}C_3H_3^+$	0.25	1.816×10^{-9}	0.2211	5.43×10^{-10}	5
$CH_2CCH + Si^+ \rightarrow H + SiC_3H_2^+$	1	1.362×10^{-9}	0.2211	1.63×10^{-9}	5
$CH_2CCH + H_3^+ \rightarrow H_2 + C_3H_4^+$	1	3.296×10^{-9}	0.2211	3.95×10^{-9}	5
$CH_2CCH + HCO^+ \rightarrow CO + C_3H_4^+$	1	1.349×10^{-9}	0.2211	1.61×10^{-9}	5
$CH_2CCH + H_3O + \rightarrow H_2O + C_3H_4^+$	1	1.539×10^{-9}	0.2211	1.84×10^{-9}	5
$CH_2CCH + CH_3^+ \rightarrow H + C_4H_5^+$	1	1.671×10^{-9}	0.2211	2.00×10^{-9}	5
$CH_2CCH + C_2H_2^+ \rightarrow H_2 + C_5H_3^+$	0.25	1.393×10^{-9}	0.2211	4.17×10^{-10}	5
$CH_2CCH + C_2H_2^+ \rightarrow H + C_5H_4^+$	0.25	1.393×10^{-9}	0.2211	4.17×10^{-10}	5
$CH_2CCH + C_2H_2^+ \rightarrow C_2H_2 + c\text{-}C_3H_3^+$	0.25	1.393×10^{-9}	0.2211	4.17×10^{-10}	5
$CH_2CCH + C_2H_2^+ \rightarrow C_2H_2 + l\text{-}C_3H_3^+$	0.25	1.393×10^{-9}	0.2211	4.17×10^{-10}	5
$CH_2CCH + C_2H_3^+ \rightarrow C_2H_2 + C_3H_4^+$	0.33	1.377×10^{-9}	0.2211	5.50×10^{-10}	5
$CH_2CCH + C_2H_3^+ \rightarrow H_2 + C_5H_4^+$	0.33	1.377×10^{-9}	0.2211	5.50×10^{-10}	5
$CH_2CCH + C_2H_3^+ \rightarrow H + C_5H_5^+$	0.33	1.377×10^{-9}	0.2211	5.50×10^{-10}	5
$CH_2CCH + c\text{-}C_3H_2^+ \rightarrow H + C_6H_4^+$	1	1.254×10^{-9}	0.2211	1.50×10^{-9}	5
$CH_2CCH + l\text{-}C_3H_2^+ \rightarrow H + C_6H_4^+$	1	1.254×10^{-9}	0.2211	1.50×10^{-9}	5
$CH_2CCH + C_4H^+ \rightarrow H + C_7H_3^+$	1	1.180×10^{-9}	0.2211	1.41×10^{-9}	5
$CH_2CCH + C_2H_4^+ \rightarrow C_2H_4 + c\text{-}C_3H_3^+$	0.25	1.362×10^{-9}	0.2211	4.08×10^{-10}	5
$CH_2CCH + C_2H_4^+ \rightarrow C_2H_4 + l\text{-}C_3H_3^+$	0.25	1.362×10^{-9}	0.2211	4.08×10^{-10}	5
$CH_2CCH + C_2H_4^+ \rightarrow CH_4 + C_4H_3^+$	0.25	1.362×10^{-9}	0.2211	4.08×10^{-10}	5
$CH_2CCH + C_2H_4^+ \rightarrow H_2 + C_5H_5^+$	0.25	1.362×10^{-9}	0.2211	4.08×10^{-10}	5
$CH_2CCH + c\text{-}C_3H_3^+ \rightarrow H_2 + C_6H_4^+$	0.50	1.246×10^{-9}	0.2211	7.46×10^{-10}	5
$CH_2CCH + c\text{-}C_3H_3^+ \rightarrow H + C_6H_5^+$	0.50	1.246×10^{-9}	0.2211	7.46×10^{-10}	5
$CH_2CCH + l\text{-}C_3H_3^+ \rightarrow H_2 + C_6H_4^+$	0.50	1.246×10^{-9}	0.2211	7.46×10^{-10}	5
$CH_2CCH + l\text{-}C_3H_3^+ \rightarrow H + C_6H_5^+$	0.50	1.246×10^{-9}	0.2211	7.46×10^{-10}	5
$CH_2CCH + C_4H_2^+ \rightarrow H_2 + C_7H_3^+$	0.50	1.175×10^{-9}	0.2211	7.03×10^{-10}	5
$CH_2CCH + C_4H_2^+ \rightarrow H + C_7H_4^+$	0.50	1.175×10^{-9}	0.2211	7.03×10^{-10}	5
$CH_2CCH + C_4H_3^+ \rightarrow H_2 + C_7H_4^+$	0.50	1.170×10^{-9}	0.2211	7.00×10^{-10}	5
$CH_2CCH + C_4H_3^+ \rightarrow H + C_7H_5^+$	0.50	1.170×10^{-9}	0.2211	7.00×10^{-10}	5
$CH_2CCH + C_5H_2^+ \rightarrow H_2 + C_8H_3^+$	0.50	1.124×10^{-9}	0.2211	6.73×10^{-10}	5
$CH_2CCH + C_5H_2^+ \rightarrow H + C_8H_4^+$	0.50	1.124×10^{-9}	0.2211	6.73×10^{-10}	5
$CH_2CCH + C_6H_2^+ \rightarrow H_2 + C_9H_3^+$	0.50	1.088×10^{-9}	0.2211	6.52×10^{-10}	5
$CH_2CCH + C_6H_2^+ \rightarrow H_2 + C_9H_3^+$	0.50	1.088×10^{-9}	0.2211	6.52×10^{-10}	5

Note.

[a] The rate constants for reactions with formula 5 are calculated using the ion-polar formula 2, $k = \alpha\beta\left(1 + 0.0967\gamma\left(\frac{300}{T}\right)^{1/2} + \frac{\gamma^2}{10.526}\frac{300}{T}\right)$. α is the branching ratio, β is the Langevin rate in units of $cm^3\ s^{-1}$ given by the expression $\beta = 2\pi e\sqrt{\frac{\alpha}{\mu}}$, and $\gamma = x = \frac{\mu_D}{\sqrt{2\alpha k_B T}}$ is a unitless correction term based on the dipole moment and polarizability of the neutral species. See Table 2 of the main text for the dipole moment and polarizability values used in these calculations.

Table 6
Ion–Molecule Reactions of CN-substituted Species

Reactions	α	β	γ (K)	k (10 K) (cm^3 s^{-1})	Formula[a,b]
1-cyano propargyl (CNCHCCH)					
CNCHCCH + H^+ → CN^+ + CH_2CCH	1.597×10^{-8}	−0.5	0	8.75×10^{-8}	3
CNCHCCH + C^+ → C_2N^+ + l-C_3H_2	4.985×10^{-9}	−0.5	0	2.73×10^{-8}	3
CNCHCCH + He^+ → He + CN^+ + l-C_3H_2	8.167×10^{-9}	−0.5	0	4.47×10^{-8}	3
H + CH_2CCH → CH_3CCH + $h\nu$	9.361×10^{-9}	−0.5	0	5.13×10^{-8}	3
CNCHCCH + HCO^+ → HCO + CN^+ + l-C_3H_2	3.547×10^{-9}	−0.5	0	1.94×10^{-8}	3
CNCHCCH + H_3O + →H_2O + HCN^+ + l-C_3H_2	4.140×10^{-9}	−0.5	0	2.27×10^{-8}	3
Propargyl cyanide ($CNCH_2CCH$)					
$CNCH_2CCH$ + H^+ → HCN^+ + CH_2CCH	1.00	6.299×10^{-9}	4.683	8.09×10^{-8}	4
$CNCH_2CCH$ + He^+ → He + CN^+ + CH_2CCH	1.00	3.220×10^{-9}	4.683	4.14×10^{-8}	4
$CNCH_2CCH$ + C^+ → C_2N^+ + CH_2CCH	1.00	1.964×10^{-9}	4.683	2.52×10^{-8}	4
$CNCH_2CCH$ + H_3^+ → H_2 + HCN^+ + CH_2CCH	1.00	3.691×10^{-9}	4.683	4.74×10^{-8}	4
$CNCH_2CCH$ + HCO^+ → HCO + CN^+ + CH_2CCH	1.00	1.396×10^{-9}	4.683	1.79×10^{-8}	4
$CNCH_2CCH$ + H_3O^+ → H_2O + HCN^+ + CH_2CCH	1.00	1.630×10^{-9}	4.683	2.09×10^{-8}	4
Cyanoallene (CH_2CCHCN)					
CH_2CCHCN + H^+ → HCN^+ + CH_2CCH	1.00	6.707×10^{-9}	5.213	9.55×10^{-8}	4
CH_2CCHCN + He^+ → He + CN^+ + CH_2CCH	1.00	3.429×10^{-9}	5.213	4.88×10^{-8}	4
CH_2CCHCN + C^+ → C_2N^+ + CH_2CCH	1.00	2.091×10^{-9}	5.213	2.98×10^{-8}	4
CH_2CCHCN + H_3^+ → H_2 + HCN^+ + CH_2CCH	1.00	3.931×10^{-9}	5.213	5.59×10^{-8}	4
CH_2CCHCN + HCO^+ → HCO + CN^+ + CH_2CCH	1.00	1.486×10^{-9}	5.213	2.12×10^{-8}	4
CH_2CCHCN + H_3O^+ → H_2O + HCN^+ + CH_2CCH	1.00	1.736×10^{-9}	5.213	2.47×10^{-8}	4
Cyanovinylacetylene (CNCHCHCCH)					
C_4H_3CN + H^+ → HCN^+ + CH_2CCH + C	1.649×10^{-8}	−0.5	0	9.03×10^{-8}	3
C_4H_3CN + He^+ → He + CN^+ + CH_2CCH + C	8.404×10^{-9}	−0.5	0	4.60×10^{-8}	3
C_4H_3CN + C^+ → C_2N^+ + CH_2CCH + C	5.086×10^{-9}	−0.5	0	2.79×10^{-8}	3
C_4H_3CN + H_3^+ → CH_2 + HCN^+ + CH_2CCH	9.644×10^{-9}	−0.5	0	5.28×10^{-8}	3
C_4H_3CN + HCO^+ → HCO + CN^+ + CH_2CCH + C	3.570×10^{-9}	−0.5	0	1.96×10^{-8}	3
C_4H_3CN + H_3O^+ → H_2O + HCN^+ + CH_2CCH + C	4.198×10^{-9}	−0.5	0	2.30×10^{-8}	3

Notes.

[a] The rate constants for reactions with formula 4 are calculated using the ion-polar formula 1, $k = \alpha\beta\left(0.62 + 0.4767\gamma\left(\frac{300}{T}\right)^{1/2}\right)$, where α is the branching ratio, $\beta = 2\pi e\sqrt{\frac{\alpha}{\mu}}$ is the Langevin rate in units of cm^3 s^{-1}, and $\gamma = x = \frac{\mu_D}{\sqrt{2\alpha k_B T}}$ is a unitless correction term based on the dipole moment and polarizability of the neutral species.

[b] Reactions with formula 3 are calculated using the modified Arrhenius formula, $k = \alpha(T/300)^{\beta}e^{-\gamma/T}$. Here α is in units of cm^3 s^{-1} and is calculated as a portion of the Langevin rate multiplied by the dipole-correction term x, $\alpha = 0.47672 \times 2\pi e\sqrt{\frac{\alpha}{\mu}}x$. β is a unitless temperature dependence term, and γ is the activation energy in K.

Appendix C
Neutral–Neutral Reactions

Table 7 contains new and updated rate coefficients for neutral–neutral gas-phase reactions involving CH_2CCH_2, CH_3CCH, and CH_2CCH. Table 8 contains new and updated rate information for grain reactions pertaining to C_3H_n species.

Table 7

Related Neutral–Neutral Reactions

Reactions[a]	α (cm^3 s^{-1})	β	γ (K)	k (10 K) (cm^3 s^{-1})[b]	References
CH_2CCH_2 reactions:					
$^*C_2H_4 + CH \rightarrow H + CH_2CCH_2$	2.74×10^{-10}	0	0	2.74×10^{-10}	23 K rate constant from Canosa et al. (1997), with 70% branching ratio from Goulay et al. (2009)
$^*H + CH_2CCH \rightarrow CH_2CCH_2 + h\nu$	1.00×10^{-13}	−1.50	0	1.64×10^{-11}	Rate constant and branching ratios from Loison et al. (2017), based on Hébrard et al. (2013), with a slightly larger rate and 50% branching ratio
$^*C + CH_2CCH_2 \rightarrow H + C_4H_3$	3.50×10^{-10}	−0.01	0	3.62×10^{-10}	Rate constant from Chastaing et al. (2000) and room-temperature products from Loison & Bergeat (2004)
$^*CCH + CH_2CCH_2 \rightarrow CH_3C_4H + H$	3.00×10^{-10}	0	0	3.00×10^{-10}	Rate constant from Loison et al. (2017) based on measurements by Carty et al. (2001)
$^*CH + CH_2CCH_2 \rightarrow CH_2CHC_2H + H$[c]	4.20×10^{-10}	0	0	4.20×10^{-10}	Rate constant from Daugey et al. (2005)
$^*CN + CH_2CCH_2 \rightarrow CH_2CCHCN + H$	3.69×10^{-10}	0	0	3.69×10^{-10}	Temperature-independent rate constant recommended by Carty et al. (2001), with branching ratios from Balucani et al. (2002)
$^*CN + CH_2CCH_2 \rightarrow CNCH_2CCH + H$	4.10×10^{-11}	0	0	3.00×10^{-10}	
CH_3CCH reactions:					
$CH + C_2H_4 \rightarrow CH_3CCH + H$	1.12×10^{-10}	0	0	1.12×10^{-10}	23 K rate constant from Canosa et al. (1997), with 30% branching ratio from Goulay et al. (2009)
$^*H + CH_2CCH \rightarrow CH_3CCH + h\nu$	1.00×10^{-13}	−1.50	0	1.64×10^{-11}	Rate constant and branching ratios from Loison et al. (2017), based on Hébrard et al. (2013), with a slightly larger rate and 50% branching ratio
$C + CH_3CCH \rightarrow H + C_4H_3$	2.30×10^{-10}	−0.11	0	3.34×10^{-10}	Rate constant from Chastaing et al. (2000) and branching ratios from Loison & Bergeat (2004), assuming 15% H_2 loss channel
$C + CH_3CCH \rightarrow H_2 + C_4H_2$	4.05×10^{-11}	−0.11	0	5.88×10^{-11}	
$CH + CH_3CCH \rightarrow CH_2CHC_2H + H$[c]	4.20×10^{-10}	0	0	4.20×10^{-10}	Rate constant from Daugey et al. (2005)
$^*CCH + CH_3CCH \rightarrow CH_3C_4H + H$	3.00×10^{-10}	0	0	3.00×10^{-10}	Rate constant from Loison et al. (2017) based on measurements by Carty et al. (2001)
$^*CN + CH_3CCH \rightarrow HC_3N + CH_3$	2.71×10^{-10}	0	0	2.71×10^{-10}	Rate constant from Carty et al. (2001) and branching ratios from Abeysekera et al. (2015)
$^*CN + CH_3CCH \rightarrow CH_3C_3N + H$	9.02×10^{-11}	0	0	9.02×10^{-11}	
$^*CN + CH_3CCH \rightarrow HCN + CH_2CCH$	4.92×10^{-11}	0	0	4.92×10^{-11}	
$^*CCH + CH_3 \rightarrow H + CH_2CCH$	1.00×10^{-10}	0	0	1.00×10^{-10}	Rate estimated by Loison et al. (2017), with H elimination assumed as major product channel
$^*C_2 + CH_4 \rightarrow CH_2CCH + H$	1.30×10^{-11}	0	0	1.30×10^{-11}	23 K rate constant from Canosa et al. (2007), assuming H-elimination product channel
$C + CH_2CCH \rightarrow H + C_4H_2$	2.00×10^{-10}	0	0	2.00×10^{-10}	Estimated in Loison et al. (2017) based on capture theory approach described in Loison et al. (2014)
$N + CH_2CCH \rightarrow H_2 + HC_3N$	5.00×10^{-11}	0	0	5.00×10^{-11}	Rate and products estimated by Loison et al. (2017) based on $N + C_2H_3$ reaction
$^*N + CH_2CCH \rightarrow C_2H_2 + HCN$	5.00×10^{-11}	0	0	5.00×10^{-10}	
$O + CH_2CCH \rightarrow CO + C_2H_3$	5.00×10^{-11}	0	0	5.00×10^{-11}	Temperature-independent Rate constant from Slagle et al. (1991), with branching ratios estimated by Loison et al. (2017) based on calculations by Lee et al. (2006)
$O + CH_2CCH \rightarrow HCO + C_2H_2$	2.00×10^{-11}	0	0	2.00×10^{-11}	
$^*O + CH_2CCH \rightarrow OH + c\text{-}C_3H_2$	1.00×10^{-11}	0	0	1.00×10^{-11}	
$^*O + CH_2CCH \rightarrow HCCCHO + H$[d]	1.60×10^{-10}	0	0	1.60×10^{-10}	
$^*OH + CH_2CCH \rightarrow C_2H_3 + HCO$	6.00×10^{-11}	0	0	6.00×10^{-11}	Rate constant from Hansen et al. (2009) and 50/50 branching ratios assumed from Loison et al. (2017)
$^*OH + CH_2CCH \rightarrow C_2H_4 + CO$	6.00×10^{-11}	0	0	6.00×10^{-11}	
$^*CN + CH_2CCH \rightarrow CNCH_2CCH + h\nu$	1.00×10^{-10}	0	0	1.00×10^{-10}	Estimated from Tennis et al. (2021)
$^*CH_2CCH + CH_2CCH \rightarrow C_6H_5 + H$	4.00×10^{-11}	0	0	4.00×10^{-11}	Room-temperature rate constant from Atkinson & Hudgens (1999), Fahr & Nayak (2000), and DeSain & Taatjes (2003)
Removed reactions:					
$CH_2CCH + H \rightarrow H_2 + c\text{-}C_3H_2$	0	0	0	0	Removed owing to sizable energy barrier as calculated by Miller & Klippenstein (2003a)
$CH_2CCH + H \rightarrow H_2 + l\text{-}C_3H_2$	0	0	0	0	

Notes.

[a] An asterisk preceding a reaction denotes that the reaction has been added to the network rather than modified.

[b] The rates of the listed neutral–neutral reactions are computed using the modified Arrhenius equation: $k = \alpha(T/300)^{\beta}e^{-\gamma/T}$, where α is a temperature-independent prefactor, β is a unitless temperature dependence parameter, and γ is the activation energy in K.

[c] The $CH + CH_3CCH$ and $CH + CH_2CCH_2$ reactions have been shown by Goulay et al. (2009) to yield CH_2CCCH_2, CH_2CHC_2H, and other isomers of C_4H_4. Since CH_2CHC_2H is the only C_4H_4 isomer currently included in the network, all of the pathways for these reactions have been combined into the formation of this isomer.

[d] Since the molecule HCCCHO is currently not included in our network, we substitute $C_3O + H + H_2$ as the products for this reaction. These do not lead directly back to CH_2CCH, avoiding a net-zero change in abundance.

Table 8

Related Neutral–Neutral Reactions on Grains

Reactions[a]	α[b]	E_a	References
s-H + s-C_3 → s-*c*-C_3H	0.60	0	Loison et al. (2017)
s-H + s-C_3 → s-*l*-C_3H	0.40	0	Loison et al. (2017)
s-H + s-*c*-C_3H → s-*c*-C_3H_2	0.80	0	Loison et al. (2017)
s-H + s-*c*-C_3H → s-*l*-C_3H_2	0.20	0	Loison et al. (2017)
s-H + s-*l*-C_3H → s-*c*-C_3H_2	0.80	0	Loison et al. (2017)
s-H + s-*l*-C_3H → s-*l*-C_3H_2	0.20	0	Loison et al. (2017)
s-H + s-*c*-C_3H_2 → s-CH_2CCH	1.00	0	Hickson et al. (2016)
s-H + s-*l*-C_3H_2 → s-CH_2CCH	1.00	0	Loison et al. (2017)
s-H + s-CH_2CCH → s-CH_3CCH	0.50	0	Loison et al. (2017)
s-H + s-CH_2CCH → s-CH_2CCH_2	0.50	0	Loison et al. (2017)
s-H_2 + s-*l*-C_3H → s-CH_2CCH	1.00	3600	Hickson et al. (2016)

Notes.

[a] In addition to these reactions forming grain products, the model also accounts for chemical desorption of 1% to form gas-phase products.

[b] The rate of reaction between two grain species *i* and *j* is calculated using the equation $k = \alpha\kappa_{ij}\left(\frac{1}{t_{\mathrm{hop}}(i)} + \frac{1}{t_{\mathrm{hop}}(j)}\right)\frac{1}{N_{\mathrm{site}}n_{\mathrm{dust}}}$, where α is the branching ratio and κ_{ij} is a parameter that depends on the activation barrier. For more information, refer to Ruaud et al. (2016).

Appendix D

Destruction Rates of CH_2CCH, CH_3CCH, and CH_2CCH_2

Figure 14 displays the rates of reaction for the major destruction mechanisms of CH_2CCH, CH_3CCH, and CH_2CCH_2 as a function of time.

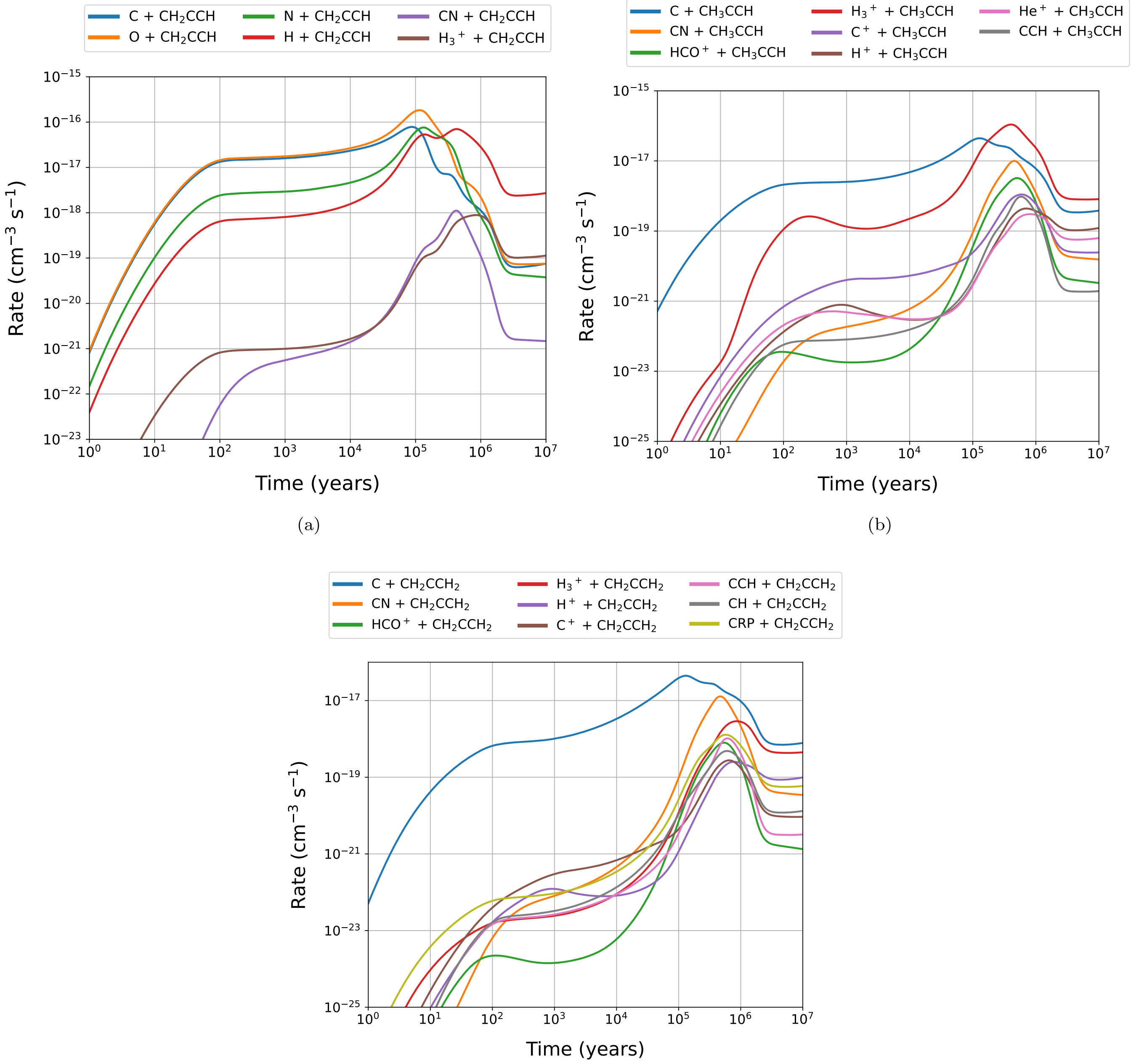

(a)

(b)

(c)

Figure 14. Reaction rates for key destruction pathways of (a) CH_2CCH, (b) CH_3CCH, and (c) CH_2CCH_2 as a function of time. For more information on these reactions, including product channels, refer to Tables 4–8.

Appendix E
Sensitivity Analyses of Remaining Reactions

Figures 15 and 16 display the sensitivity analysis results not shown in the manuscript. For each reaction, the rate constant was multiplied by a number of factors and a model performed for each factor. Figure 17 illustrates the modeled abundances of CH_2CCH, CH_3CCH, and CH_2CCH_2 for different initial C/O ratios, obtained by adjusting the initial abundance of atomic oxygen.

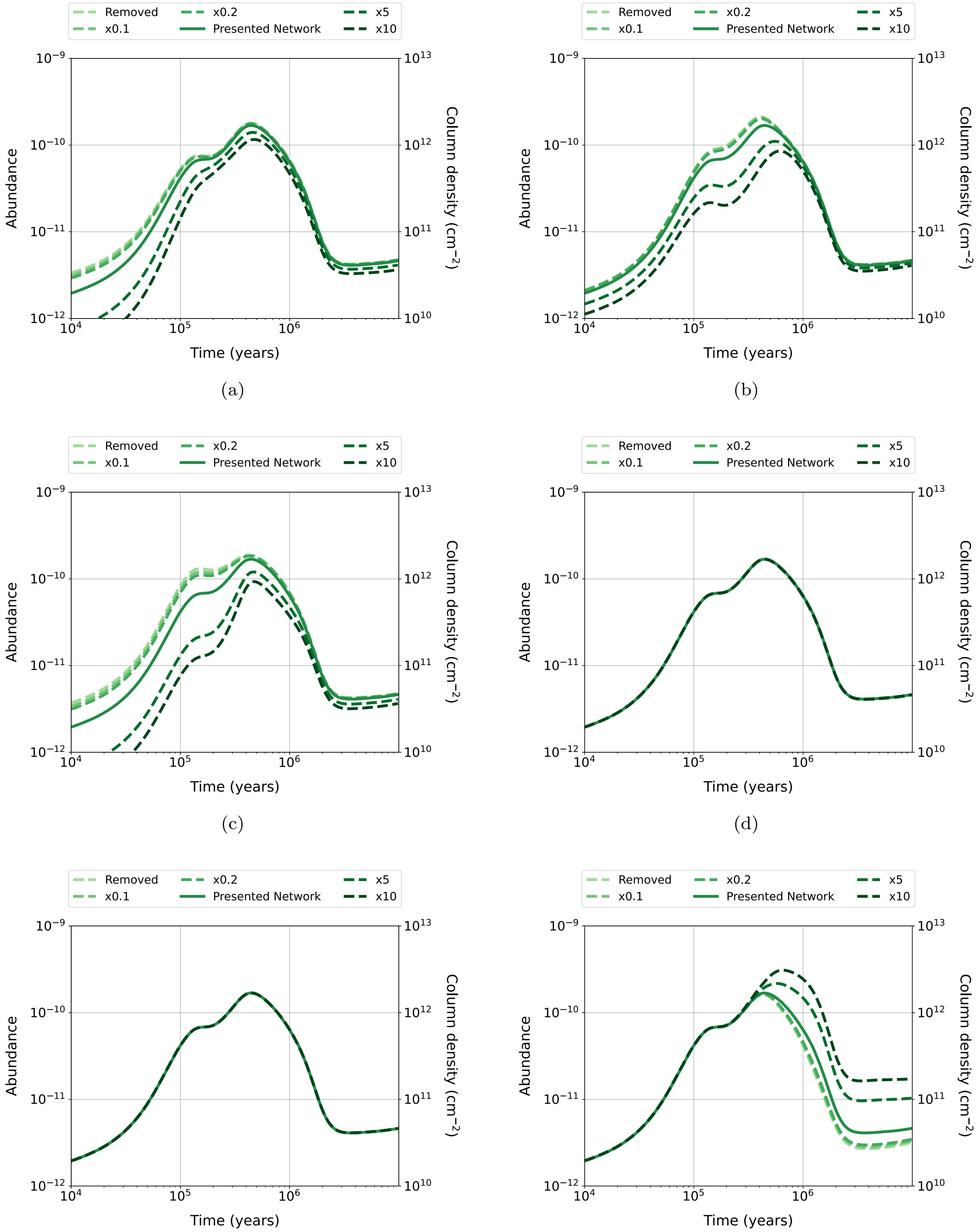

(a) (b)

(c) (d)

(e) (f)

Figure 15. Modeled abundances and column densities of CH_2CCH for different values of the (a) $CH_2CCH + C$, (b) $CH_2CCH + N$, (c) $CH_2CCH + O$, (d) $CH_2CCH + OH$, (e) $CH_2CCH + CN$, and (f) $CCH + CH_3$ rate constants. The dashed lines are networks where this rate constant has been modified by the factors in the legend. The base network (presented in this paper) is shown for comparison as a solid line, as well as a network where this reaction is removed entirely. The color gradient corresponds with the magnitude of the factor of change.

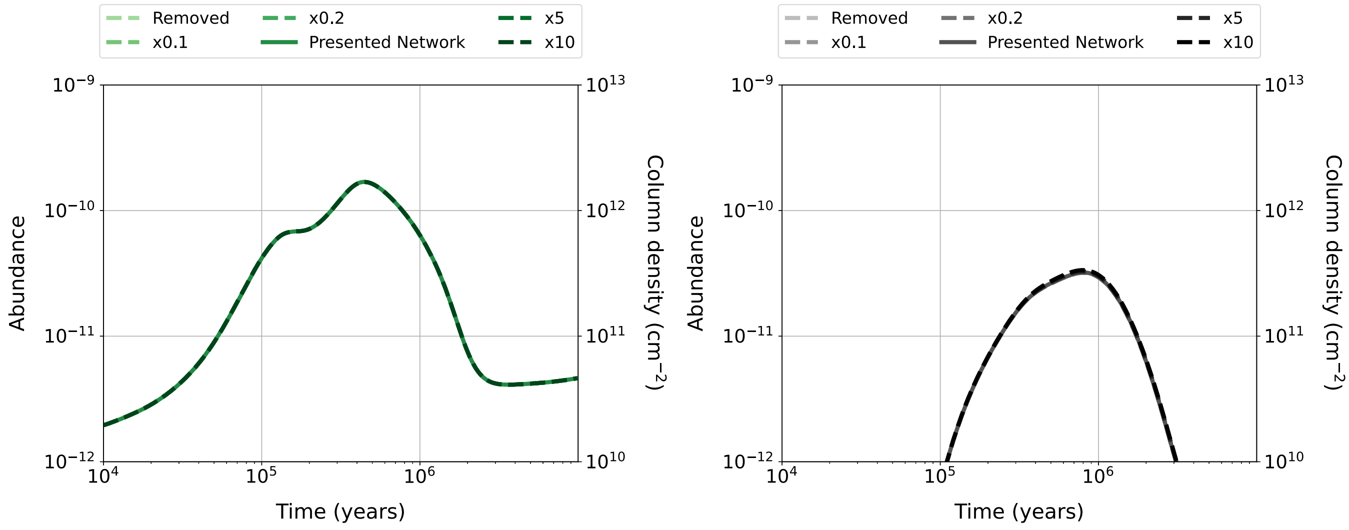

(a) (b)

Figure 16. Modeled abundances and column densities of (a) CH_2CCH and (b) C_6H_5 for different values of the $CH_2CCH + CH_2CCH$ rate constant. The dashed lines are networks where this rate constant has been modified by the factors in the legend. The base network (presented in this paper) is shown for comparison as a solid line, as well as a network where this reaction is removed entirely. The color gradient corresponds with the magnitude of the factor of change.

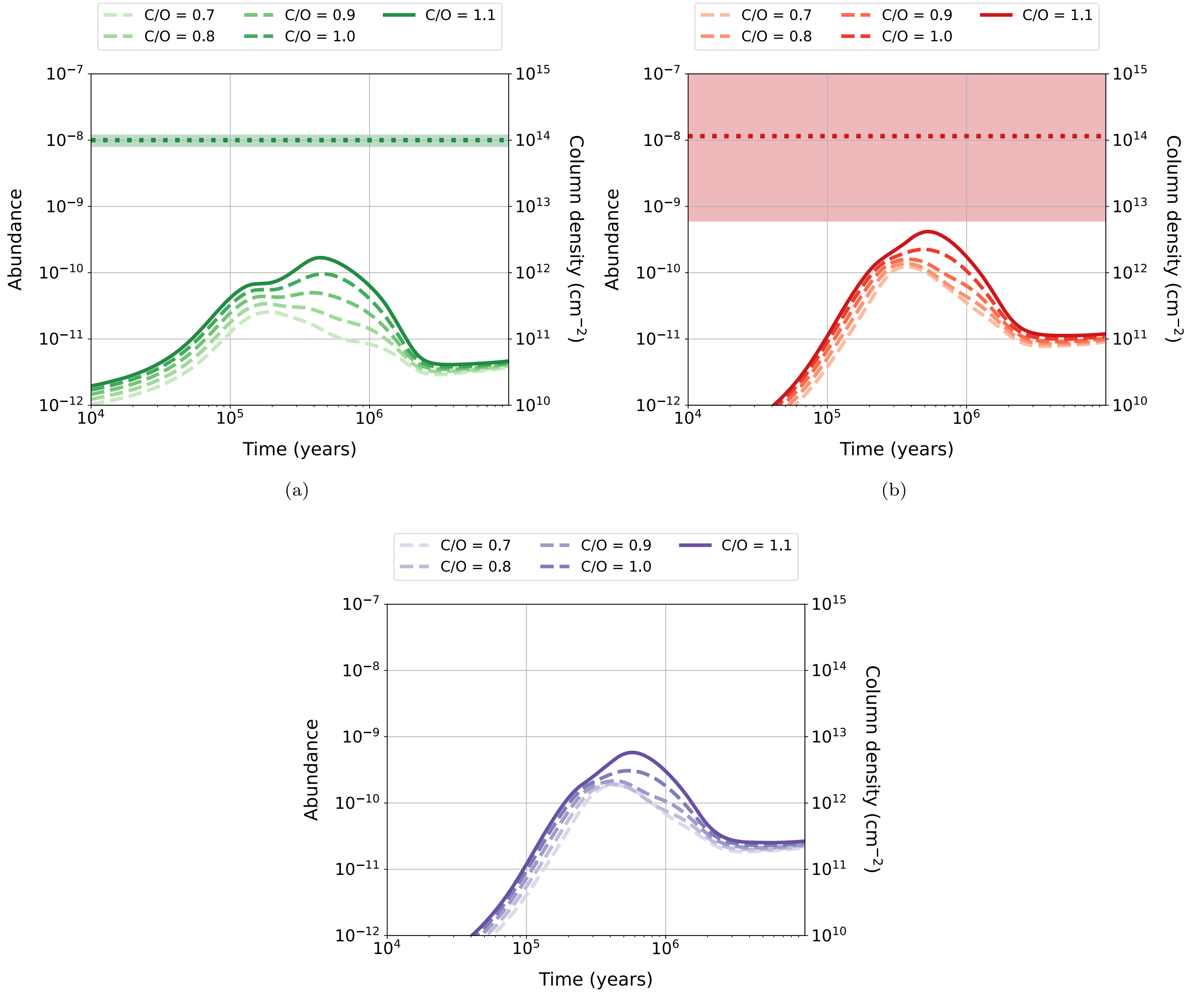

(a)

(b)

(c)

Figure 17. Modeled abundances and column densities of (a) CH_2CCH, (b) CH_3CCH, and (c) CH_2CCH_2 for different initial abundances of elemental oxygen. The solid line indicates the base model with a C/O ratio of 1.1, while the dashed lines indicate models with variations in C/O ratio. The color gradient corresponds with the magnitude of the C/O ratio. The dotted line represents the observed column density in TMC-1, with the shaded area signifying an error of 1σ.

ORCID iDs

Alex N. Byrne https://orcid.org/0000-0002-4593-518X
Ci Xue https://orcid.org/0000-0003-2760-2119
Ilsa R. Cooke https://orcid.org/0000-0002-0850-7426
Michael C. McCarthy https://orcid.org/0000-0001-9142-0008
Brett A. McGuire https://orcid.org/0000-0003-1254-4817

References

Abeysekera, C., Joalland, B., Ariyasingha, N., et al. 2015, J. Phys. Chem. Lett., 6, 1599
Agúndez, M., Cabezas, C., Tercero, B., et al. 2021, A&A, 647, L10
Agúndez, M., Marcelino, N., Cabezas, C., et al. 2022, A&A, 657, A96
Angelova, G., Novotny, O., Mitchell, J. B. A., et al. 2004, IJMSp, 235, 7
Atkinson, D. B., & Hudgens, J. W. 1999, JPCA, 103, 4242
Balucani, N., Asvany, O., Huang, L. C. L., et al. 2000, ApJ, 545, 892
Balucani, N., Asvany, O., Kaiser, R.-I., & Osamura, Y. 2002, JPCA, 106, 4301
Behmard, A., Fayolle, E. C., Graninger, D. M., et al. 2019, ApJ, 875, 73
Bergeat, A., & Loison, J.-C. 2001, PCCP, 3, 2038
Berné, O., Montillaud, J., & Joblin, C. 2015, A&A, 577, A133
Bouchy, A., Demaison, J., Roussy, G., & Barriol, J. 1973, JMoSt, 18, 211
Broten, N. W., MacLeod, J. M., Avery, L. W., et al. 1984, ApJL, 276, L25
Burkhardt, A. M., Lee, K. L. K., Changala, P. B., et al. 2021a, ApJL, 913, L18
Burkhardt, A. M., Loomis, R. A., Shingledecker, C. N., et al. 2021b, NatAs, 5, 181
Cabezas, C., Agúndez, M., Marcelino, N., et al. 2021, A&A, 654, L9
Cabezas, C., Nakajima, M., Chang, C. H., et al. 2022, A&A, 657, A24
Canosa, A., Páramo, A., Le Picard, S. D., & Sims, I. R. 2007, Icar, 187, 558
Canosa, A., Sims, I. R., Travers, D., Smith, I. W. M., & Rowe, B. R. 1997, A&A, 323, 644
Carty, D., Le Page, V., Sims, I. R., & Smith, I. W. M. 2001, CPL, 344, 310
Caster, K. L., Donnellan, Z. N., Selby, T. M., & Goulay, F. 2019, JPCA, 123, 5692
Cernicharo, J., Fuentetaja, R., Agúndez, M., et al. 2022, A&A, 663, L9
Chabot, M., Béroff, K., Dartois, E., Pino, T., & Godard, M. 2019, ApJ, 888, 17
Chastaing, D., James, P. L., Sims, I. R., & Smith, I. W. M. 1999, PCCP, 1, 2247
Chastaing, D., Le Picard, S. D., Sims, I. R., et al. 2000, CPL, 331, 170
Chastaing, D., Le Picard, S. D., Sims, I. R., & Smith, I. W. M. 2001, A&A, 365, 241
Chin, C.-H., Chen, W.-K., Huang, W.-J., Lin, Y.-C., & Lee, S.-H. 2012, JPCA, 116, 7615
Cooke, I. R., Gupta, D., Messinger, J. P., & Sims, I. R. 2020, ApJL, 891, L41
Cooke, I. R., & Sims, I. R. 2019, ECS, 3, 1109

da Silva, G., & Bozzelli, J. W. 2009, JPCA, 113, 12045

Daugey, N., Caubet, P., Retail, B., et al. 2005, PCCP, 7, 2921

Decker, B. K., & Macdonald, R. G. 2003, JPCA, 107, 9137

DeSain, J. D., & Taatjes, C. A. 2003, JPCA, 107, 4843

Doddipatla, S., Galimova, G. R., Wei, H., et al. 2021, SciA, 7, eabd4044

Duley, W. W. 2006, FaDi, 133, 415

Fahr, A., & Nayak, A. 2000, Int. J. Chem. Kinet, 32, 118

Florescu-Mitchell, A. I., & Mitchell, J. B. A. 2006, PhR, 430, 277

Fournier, J. A., Shuman, N. S., Melko, J. J., Ard, S. G., & Viggiano, A. A. 2013, JChPh, 138, 154201

Friedman, L. 1968, ARPC, 19, 273

Fuente, A., Rivière-Marichalar, P., Beitia-Antero, L., et al. 2023, A&A, 670, A114

Garrod, R. T., Wakelam, V., & Herbst, E. 2007, A&A, 467, 1103

Georgievskii, Y., Miller, J. A., & Klippenstein, S. J. 2007, PCCP, 9, 4259

Geppert, W. D., Naulin, C., Costes, M., et al. 2003, JChPh, 119, 10607

Geppert, W. D., Thomas, R., Ehlerding, A., et al. 2004, IJMSp, 237, 25

Goulay, F., Trevitt, A. J., Meloni, G., et al. 2009, J. Am. Chem. Soc., 131, 993

Graedel, T. E., Langer, W. D., & Frerking, M. A. 1982, ApJS, 48, 321

Gratier, P., Majumdar, L., Ohishi, M., et al. 2016, ApJS, 225, 25

Hansen, N., Miller, J. A., Westmoreland, P. R., et al. 2009, CoFl, 156, 2153

Hays, B. M., Gupta, D., Guillaume, T., et al. 2022, NatCh, 14, 811

Hébrard, E., Dobrijevic, M., Bénilan, Y., & Raulin, F. 2006, J. Photochem. Photobiol. C, 7, 211

Hébrard, E., Dobrijevic, M., Loison, J. C., et al. 2013, A&A, 552, A132

Hébrard, E., Dobrijevic, M., Pernot, P., et al. 2009, JPCA, 113, 11227

Hickson, K. M., Wakelam, V., & Loison, J.-C. 2016, MolAs, 3, 1

Hincelin, U., Wakelam, V., Hersant, F., et al. 2011, A&A, 530, A61

Jenkins, E. B. 2009, ApJ, 700, 1299

Jiménez, E., Antiñolo, M., Ballesteros, B., Canosa, A., & Albaladejo, J. 2016, PCCP, 18, 2183

Jones, B. M., Zhang, F., Kaiser, R. I., et al. 2011, PNAS, 108, 452

Kaiser, R. I., & Hansen, N. 2021, JPCA, 125, 3826

Krasnoukhov, V. S., Pivovarov, P. S., Zagidullin, M. V., et al. 2022, ARep, 66, 811

Küpper, J., Merritt, J. M., & Miller, R. E. 2002, JChPh, 117, 647

Larsson, M., Ehlerding, A., Geppert, W. D., et al. 2005, JChPh, 122, 156101

Le, T. N., Lee, H.-y., Mebel, A. M., & Kaiser, R. I. 2001, JPCA, 105, 1847

Lee, H., Nam, M.-J., & Choi, J.-H. 2006, JChPh, 124, 044311

Lee, K. L. K., Loomis, R. A., Burkhardt, A. M., et al. 2021, ApJL, 908, L11

Loison, J.-C., Agúndez, M., Wakelam, V., et al. 2017, MNRAS, 470, 4075

Loison, J.-C., & Bergeat, A. 2004, PCCP, 6, 5396

Loison, J.-C., Wakelam, V., Hickson, K. M., Bergeat, A., & Mereau, R. 2014, MNRAS, 437, 930

Loomis, R. A., Burkhardt, A. M., Shingledecker, C. N., et al. 2021, NatAs, 5, 188

Lovas, F. J., Remijan, A. J., Hollis, J. M., Jewell, P. R., & Snyder, L. E. 2006, ApJL, 637, L37

Mandal, M., Ghosh, S., & Maiti, B. 2018, JPCA, 122, 3556

Marcelino, N., Tercero, B., Agúndez, M., & Cernicharo, J. 2021, A&A, 646, L9

McCarthy, M. C., Lee, K. L. K., Loomis, R. A., et al. 2021, NatAs, 5, 176

McGuire, B. A., Burkhardt, A. M., Kalenskii, S., et al. 2018, Sci, 359, 202

McGuire, B. A., Burkhardt, A. M., Loomis, R. A., et al. 2020, ApJL, 900, L10

McGuire, B. A., Loomis, R. A., Burkhardt, A. M., et al. 2021, Sci, 371, 1265

McNaughton, D., Romeril, N. G., Lappert, M. F., & Kroto, H. W. 1988, JMoSp, 132, 407

Miller, J. A., & Klippenstein, S. J. 2003a, JPCA, 107, 2680

Miller, J. A., & Klippenstein, S. J. 2003b, JPCA, 107, 7783

Miller, J. A., Klippenstein, S. J., Georgievskii, Y., et al. 2010, JPCA, 114, 4881

Miller, J. A., & Melius, C. F. 1992, CoFl, 91, 21

Morozov, A. N., & Mebel, A. M. 2020, PCCP, 22, 6868

Narendrapurapu, B. S., Simmonett, A. C., Schaefer, H. F. I., Miller, J. A., & Klippenstein, S. J. 2011, JPCA, 115, 14209

Neufeld, D. A., Wolfire, M. G., & Schilke, P. 2005, ApJ, 628, 260

Parker, D. S. N., Zhang, F., Kim, Y. S., et al. 2012, PNAS, 109, 53

Pratap, P., Dickens, J. E., Snell, R. L., et al. 1997, ApJ, 486, 862

Quan, D., & Herbst, E. 2007, A&A, 474, 521

Rodríguez-Baras, M., Fuente, A., Riviére-Marichalar, P., et al. 2021, A&A, 648, A120

Rowe, B. R., Dupeyrat, G., Marquette, J. B., & Gaucherel, P. 1984, JChPh, 80, 4915

Ruaud, M., Wakelam, V., & Hersant, F. 2016, MNRAS, 459, 3756

Siebert, M. A., Lee, K. L. K., Remijan, A. J., et al. 2022, ApJ, 924, 21

Sita, M. L., Changala, P. B., Xue, C., et al. 2022, ApJL, 938, L12

Slagle, I. R., Gmurczyk, G. W., Batt, L., & Gutman, D. 1991, Symp., Int., Combust., 23, 115

Snell, R. L., Langer, W. D., & Frerking, M. A. 1982, ApJ, 255, 149

Spitzer, L., Jr., & Tomasko, M. G. 1968, ApJ, 152, 971

Su, T., & Chesnavich, W. J. 1982, JChPh, 76, 5183

Tennis, J., Loison, J.-C., & Herbst, E. 2021, ApJ, 922, 133

Tielens, A. 2008, ARA&A, 46, 289

Villadsen, T., Ligterink, N. F. W., & Andersen, M. 2022, A&A, 666, A45

Wakelam, V., & Herbst, E. 2008, ApJ, 680, 371

Wakelam, V., Herbst, E., & Selsis, F. 2006, A&A, 451, 551

Wakelam, V., Loison, J.-C., Herbst, E., et al. 2015, ApJS, 217, 20

Wakelam, V., Loison, J. C., Mereau, R., & Ruaud, M. 2017, MolAs, 6, 22

Woon, D. E., & Herbst, E. 2009, ApJS, 185, 273

Xue, C., Willis, E. R., Loomis, R. A., et al. 2020, ApJL, 900, L9

Zhao, L., Lu, W., Ahmed, M., et al. 2021, SciA, 7, eabf0360